# Diagnosis of a North American Polar/Subtropical Jet Superposition Employing Piecewise Potential Vorticity Inversion

*By*

ANDREW C. WINTERS[1*] and JONATHAN E. MARTIN[2]

[1]Department of Atmospheric and Environmental Sciences
University at Albany – State University of New York
Albany, NY 12222

[2]Department of Atmospheric and Oceanic Sciences
University of Wisconsin-Madison
Madison, WI 53706

Submitted for publication in *Monthly Weather Review*
11 July 2016
Submitted revised version
27 October 2016

[*] *Corresponding author address:* Andrew C. Winters, Dept. of Atmospheric and Environmental Sciences, University at Albany, SUNY, 1400 Washington Ave., Albany, NY 12222. E-mail: acwinters@albany.edu

[1] Throughout this study, tropopause specifically refers to the dynamic tropopause, which is defined as a surface of

## Abstract

The polar jet (PJ) and subtropical jet (STJ) often reside in different climatological latitude bands. On occasion, the meridional separation between the two jets can vanish, resulting in a relatively rare vertical superposition of the PJ and STJ. A large-scale environment conducive to jet superposition can be conceptualized as one that facilitates the simultaneous advection of tropopause-level potential vorticity (PV) perturbations along the polar and subtropical waveguides towards middle latitudes. Once these PV perturbations are transported into close proximity to one another, interactions between tropopause-level, lower-tropospheric, and diabatically-generated PV perturbations work to restructure the tropopause into the two-step, pole-to-equator tropopause structure characteristic of a jet superposition.

This study employs piecewise PV inversion to diagnose the interactions between large-scale PV perturbations throughout the development of a jet superposition during the 18–20 December 2009 Mid-Atlantic Blizzard. While the influence of PV perturbations in the lower troposphere as well as those generated via diabatic processes were notable in this case, tropopause-level PV perturbations played the most substantial role in restructuring the tropopause prior to jet superposition. A novel PV partitioning scheme is presented that isolates PV perturbations associated with the PJ and STJ, respectively. Inversion of the jet-specific PV perturbations suggests that these separate features make distinct contributions to the restructuring of the tropopause that characterizes the development of a jet superposition.

## 1. Introduction

The atmosphere typically exhibits the three-step pole-to-equator tropopause structure shown in Fig. 1a, with each break in the tropopause height associated with a jet stream[1]. The polar jet (PJ) stream resides at middle latitudes in the break between the polar (~350 hPa) and subtropical (~250 hPa) tropopauses and is situated atop the strongly baroclinic, tropospheric-deep polar front (e.g., Palmén and Newton 1948; Namias and Clapp 1949; Newton 1954; Palmén and Newton 1969; Keyser and Shapiro 1986; Shapiro and Keyser 1990). The subtropical jet (STJ) stream is located equatorward of the PJ (~30°N in the Northern Hemisphere) in the break between the subtropical tropopause and the even higher tropical tropopause (~100 hPa) and is characterized by modest baroclinicity in the upper troposphere and lower stratosphere (e.g., Loewe and Radok 1950; Yeh 1950; Koteswaram 1953; Mohri 1953; Koteswaram and Parthasarathy 1954; Sutcliffe and Bannon 1954; Krishnamurti 1961; Riehl 1962).

While the separate polar and subtropical jets typically reside in different climatological latitude bands, their meridional separation occasionally vanishes, resulting in a relatively rare vertical superposition of the PJ and STJ (Christenson 2013). A vertical cross section through a jet superposition is shown in Fig. 1b, which highlights three of the primary attributes of a superposition: (1) the development of a two-step tropopause structure from polar to tropical latitudes, rather than the more common three-step structure shown in Fig. 1a, (2) a consolidation of the upper-tropospheric and lower-stratospheric baroclinicity associated with each jet into substantially narrower zones of contrast, and (3) anomalously strong wind speeds associated with the aforementioned increase in baroclinicity.

[1] Throughout this study, tropopause specifically refers to the dynamic tropopause, which is defined as a surface of constant potential vorticity (e.g., Morgan and Nielsen-Gammon 1998). In line with previous work, we select the 2-PVU surface (1 PVU = $10^{-6}$ K m$^2$ kg$^{-1}$ s$^{-1}$). The term, jet, will also be synonymous with jet streak in the text and refers to a zonally confined wind speed maximum along either the polar or subtropical waveguide.

94 The observations of the tropopause discussed with reference to Fig. 1 served as the
95 foundation for the objective identification scheme for the PJ, STJ, and superposed jets outlined in
96 Winters and Martin (2014). Employing that jet identification scheme as part of an analysis of the
97 historic 1–3 May 2010 Nashville Flood, Winters and Martin (2014) determined that the
98 development of a jet superposition was a critical component in the evolution of that flooding
99 event. A cursory reexamination of a number of other historical and recent high-impact weather
100 events over North America and the North Atlantic by the authors suggests that superposed jets
101 were a component of their evolution, as well (e.g., Defant 1959; Hoskins and Berrisford 1988;
102 Hakim et al. 1995, 1996; Bosart et al. 1996; Christenson 2013).
103 The association of jet superpositions with a class of high-impact weather events
104 motivated Winters and Martin (2016, hereafter WM16) to diagnose the development of a jet
105 superposition in two cases: the 18–20 December 2009 Mid-Atlantic Blizzard and the
106 aforementioned 1–3 May 2010 Nashville Flood. These cases demonstrated that elements of both
107 the antecedent remote and local synoptic environments are important to consider when
108 diagnosing the development of a superposition. A large-scale environment conducive to jet
109 superposition is broadly conceptualized in Fig. 2 as one that facilitates the simultaneous
110 advection of tropopause-level cyclonic and anticyclonic potential vorticity (PV) perturbations
111 from polar and tropical latitudes, respectively, and the subsequent horizontal juxtaposition of
112 those PV perturbations at middle latitudes.
113 Much attention in the literature has focused on the origin and characteristics of these
114 tropopause-level PV perturbations. Polar cyclonic PV perturbations, which have been referred to
115 as coherent tropopause disturbances (CTDs; Pyle et al. 2004), are typically located along the
116 polar waveguide, accompanied by a PJ on their equatorward flank (Fig. 2), and exhibit a

localized depression in the height of the tropopause. One particular class of CTD that has received specific attention is the tropopause polar vortex (TPV), which primarily forms as a result of an enhanced vertical gradient in radiative heating near the tropopause at polar latitudes (Cavallo and Hakim 2010). As CTDs are transported towards middle latitudes by the background flow within which they are embedded, they occasionally initiate surface cyclogenesis (e.g., Hakim et al. 1995, 1996; Pyle et al. 2004; Cavallo and Hakim 2010).

In contrast to polar latitudes, where polar cyclonic PV perturbations are manifest on the tropopause as coherent vortices, tropical anticyclonic PV perturbations are not readily identifiable on the tropopause at tropical latitudes (i.e., Morgan and Nielsen-Gammon 1998, their Fig. 2). Instead, the tropical upper-troposphere is characterized by a reservoir of uniform, low PV air that is continuously replenished by mass deposition in the upper troposphere from tropical convection. Once this tropical, low PV air is transported poleward via tropical plumes or the presence of a low-latitude trough (e.g., Liebmann and Hartmann 1984; Iskenderian 1995; Roundy et al. 2010; Fröhlich et al. 2013; Archambault et al. 2013, 2015; WM16), it becomes manifest as an anticyclonic PV perturbation along the subtropical waveguide with a STJ positioned on its poleward flank (Fig. 2). Not only are these tropical anticyclonic PV perturbations accompanied by an upper-tropospheric thermodynamic environment characterized by weak static stability, but also by the occasional presence of atmospheric rivers (Newell et al. 1992; Zhu and Newell 1998; Ralph et al. 2004) within the poleward-directed branch of their anticyclonic circulation. Consequently, the horizontal juxtaposition of polar cyclonic and tropical anticyclonic PV perturbations at middle latitudes typifies a dynamical and thermodynamic environment conducive to the production of high-impact weather.

As polar cyclonic and tropical anticyclonic PV perturbations are transported into close proximity to one another, the individual non-divergent circulations associated with each PV perturbation add constructively to produce the anomalously strong upper-tropospheric wind speeds associated with a superposed jet. In addition, mesoscale processes within the near-jet environment, such as ageostrophic transverse circulations and proximate midlatitude convection (Fig. 2), can act to locally restructure the tropopause into the two-step structure characteristic of a jet superposition (WM16). While WM16 note the relevance of dynamical structures within the remote synoptic environment to the production of a superposition, stronger emphasis is placed on the role of mesoscale processes within the near-jet environment. Consequently, a detailed understanding of the large-scale interaction between tropopause-level PV perturbations along the polar and subtropical waveguides during a jet superposition event remains unresolved.

A particularly effective way to examine the large-scale interaction between separate PV perturbations during the development of a jet superposition is to employ piecewise PV inversion, which leverages the intrinsic principles of PV conservation and invertibility (e.g., Hoskins et al. 1985; Thorpe 1985; Robinson 1988; Holopainen and Kaurola 1991; Davis and Emanuel 1991). Specifically, these principles imply that (1) the PV serves as a particularly good tracer for atmospheric motion under the assumption of adiabatic and inviscid flow and (2) knowledge of a PV perturbation at a particular time, along with a suitable balance condition, permits a recovery of the mass and thermal fields associated with that PV perturbation.

Piecewise PV inversion has been employed extensively to examine a number of different tropospheric processes. In particular, piecewise PV inversion has fostered insight into surface cyclogenesis (e.g., Davis and Emanuel 1991; Davis 1992a,b; Davis et al. 1993; Davis et al. 1996; Nielsen-Gammon and Lefevre 1996; Morgan and Nielsen-Gammon 1998), midlatitude trough

interaction (e.g., Hakim et al. 1996), tropospheric frontogenesis (e.g., Morgan 1999; Korner and Martin 2000), the development and movement of tropical cyclones (e.g., Wu and Emanuel 1995a,b; Shapiro 1996; Shapiro and Franklin 1999; McTaggart-Cowan et al. 2001; Shapiro and Möller 2003), and understanding of tropical–extratropical interactions (e.g., McTaggart-Cowan et al. 2001, 2004, Agustí-Panareda et al. 2004; Ahmadi-Givi et al. 2004; Grams et al. 2011, 2013).

The analysis performed by Wandishin et al. (2000), however, is of particular relevance when considering the application of PV inversion to diagnose the development of a jet superposition. In that study, piecewise quasi-geostrophic (QG) PV inversion was employed to examine the development of an idealized tropopause break. The analysis determined that vertical motion at the tropopause initiated the development of a tropopause break by vertically tilting an initially flat portion of the tropopause. Once the tropopause exhibited a vertical slope, the presence of a vertical shear acted to further tilt the tropopause in the vertical, completing the production of the tropopause break (Wandishin et al. 2000; their Fig. 4).

For the present work, which centers on diagnosing the vertical alignment of two distinct tropopause breaks, both differential horizontal displacement and vertical motion are likely to play important roles. As an idealized example, Fig. 3 depicts a vertical wind profile (red arrows) that would result in a poleward displacement of the subtropical tropopause break and an equatorward displacement of the polar tropopause break. This differential horizontal displacement of the two tropopause breaks may promote their vertical alignment at a later time. In addition, vertical motion (blue arrow) positioned between the polar and subtropical tropopause breaks has the capability to alter the elevation of the subtropical tropopause and contribute to the production of the two-step tropopause structure characteristic of a jet superposition (WM16).

While the nature of the interaction between tropopause-level PV perturbations along the polar and subtropical waveguides, and their role in the production of a jet superposition, is of particular interest to this study, it is also apparent that jet superposition events can be associated with surface cyclogenesis and midlatitude convection (WM16). Consequently, a holistic understanding of the process of jet superposition from a PV perspective necessitates consideration of the influence that both lower-tropospheric and diabatically-generated PV perturbations have on the production of a jet superposition, as well. With this in mind, the forthcoming analysis isolates tropopause-level, lower-tropospheric, and diabatically-generated PV perturbations during a well-established case of jet superposition analyzed by WM16. These PV perturbations are subsequently inverted in an effort to diagnose the dynamical structures that contribute the most towards restructuring the tropopause during a jet superposition event.

The remainder of this study is structured as follows. Section 2 discusses the methodology employed in this study to partition the PV distribution and to perform piecewise PV inversion. Section 3 applies piecewise PV inversion to a well-established case of jet superposition previously examined by WM16 and Section 4 finishes with a brief discussion and some conclusions.

## 2. Methodology

This study considers the development of a jet superposition during the 18–20 December 2009 Mid-Atlantic Blizzard, which was chosen to complement the analysis previously performed on this case by WM16. For more specific information on the impacts of this case, the reader is referred to WM16. Wind, temperature, geopotential height, and relative humidity data for this case was acquired from National Centers for Environmental Prediction (NCEP) Global Forecast System (GFS) analyses at 6-h intervals during the 6-day period, 0000 UTC 17 December 2009 –

208 0000 UTC 23 December 2009. The model data has a horizontal grid spacing of 1.0° × 1.0° and
209 20 vertical levels, with a vertical grid spacing of 50 hPa between 1000–50-hPa. The GFS model
210 data served as boundary conditions for performing the piecewise PV inversion. The details of the
211 inversion techniques are provided in the discussion that follows.

212 *a) PV Partitioning Scheme*

213 The degree to which insight is gained from piecewise PV inversion is highly dependent
214 upon the scheme used to partition the PV distribution. Consequently, care must be taken to
215 partition the flow into a finite number of pieces, such that each piece captures a subset of the PV
216 distribution that is associated with a particular dynamical structure. The Perturbation PV (PPV)
217 at 6-h intervals was defined as the instantaneous deviation of the full PV at a grid point from the
218 6-day Mean PV (MPV) at that same grid point. The PPV was further partitioned at each 6-h
219 interval using a slightly modified version of the three-way partition described by Korner and
220 Martin (2000).

221 A conceptual diagram illustrating this three-way partition is shown in Fig. 4a. The
222 Surface PV (SPV) isolates the PPV at grid points in the 950–850-hPa isobaric layer with a
223 relative humidity < 70%, as well as all potential temperature perturbations (calculated against a
224 6-day mean for each grid point) on the bottom boundary of the domain. The SPV is designed to
225 capture the impact of near-surface temperature perturbations that behave as PV perturbations
226 along the bottom boundary of the domain (Bretherton 1966). The Interior PV (IPV) isolates the
227 PPV at grid points in the 950–150-hPa isobaric layer with a relative humidity ≥ 70%[2]. The IPV is
228 designed to separate the diabatic creation and destruction of PV that accompanies latent heat
229 release. Finally, the Upper-Tropospheric PV (UTPV) captures the PPV at grid points in the 650–

[2] The relative humidity criterion is identical to that used by Davis (1992b) and Korner and Martin (2000). In those studies, this threshold was chosen to capture PV perturbations associated with latent heat release that may have been advected out of a region of saturated ascent and into a region of weak subsidence (e.g., subsaturated air).

100-hPa isobaric layer with a relative humidity < 70%, as well as all temperature perturbations on the top boundary of the domain. The UTPV isolates dry air of either stratospheric or upper-tropospheric origin and captures the PPV tied to dynamical structures in the middle and upper troposphere, including the PJ and STJ. Together, the SPV, IPV, and UTPV account for nearly all of the PPV within the domain, except for dry air between 800–700-hPa and nearly saturated air above 150-hPa. An examination of this residual PPV demonstrates that it is negligible and its omission does not significantly impact the analysis.

While a three-way partition of the PPV provides insight into the interaction between PV perturbations in the lower and upper troposphere and those generated via diabatic processes, it does not separate the influence of individual PV perturbations along the polar and subtropical waveguides during a jet superposition event (i.e., polar cyclonic and tropical anticyclonic PV perturbations). Consequently, an additional partitioning scheme is employed to isolate the PPV associated with the PJ and STJ, respectively. In the upper troposphere and lower stratosphere, an individual tropopause break is characterized in Fig. 4b by the horizontal juxtaposition of a positive PV perturbation on the poleward side of the tropopause break and a negative PV perturbation on the equatorward side of the tropopause break (e.g., Davies and Rossa 1998; Morgan and Nielsen-Gammon 1998; Pyle et al. 2004). The non-divergent circulations accompanying these PV perturbations subsequently combine to drive a jet that is situated parallel to its respective tropopause break. To capture these PV perturbations, the partitioning scheme isolates the PPV associated with each jet by considering the characteristic isentropic layers that contain the polar and subtropical tropopause breaks.

The isentropic layers used for the jet PV partition are subjective and are heavily dependent upon the case under consideration. For the 18–20 December 2009 Blizzard, the Polar

Jet PV (PJPV) isolates the PPV at grid points in the 305–325-K isentropic layer with a relative humidity < 70%. The implementation of a relative humidity criterion in this partition is designed to remove the influence of proximate latent heat release when determining the flow associated with the PJ and STJ. The Subtropical Jet PV (STJPV) isolates the PPV at grid points in the 325–355-K isentropic layer with a relative humidity < 70%. An examination of potential temperature on the dynamic tropopause over North America throughout the duration of this case demonstrates that the 325-K isentrope routinely intersected the subtropical tropopause step (e.g., Fig. 4b). Consequently, the 325-K surface served as a suitable isentrope to differentiate between the PJPV and STJPV.

The distribution of PJPV and STJPV within the cross section, A–A', at 0000 UTC 19 December 2009 is shown in Fig. 4c. An examination of the non-divergent wind associated with the jet-specific PV perturbations further demonstrates that the PJPV and STJPV account for a large majority of the perturbation flow associated with the PJ and STJ, respectively (not shown). While the PJPV and STJPV are not a strict partition of the UTPV, their sum closely approximates the distribution and magnitude of the UTPV. Consequently, an examination of the three-dimensional circulations associated with the PJPV and STJPV provides insight into the nature of the interaction between PV perturbations along the polar and subtropical waveguides during the development of a jet superposition.

*b) Piecewise PV Inversion Techniques*

Since substantial flow curvature and diabatic processes routinely characterize jet superposition events (WM16), an inversion of the Ertel PV (Ertel 1942) is more suitable for diagnosing the interaction between PV perturbations during a jet superposition event than QGPV inversion. For the present study, a static PV inversion was used to invert the Ertel PV for its

associated geopotential, $\phi$, and non-divergent streamfunction, $\psi$. The methodology for performing the static PV inversion is identical to that described by Davis and Emanuel (1991) and the reader is encouraged to consult that work for any technical details.

Full and piecewise static PV inversions were performed within a North American domain bounded horizontally from 130°W–50°W and 10°N–65°N and vertically by the 1000-hPa and 50-hPa isobaric surfaces. For an inversion of the full PV, the analyzed geopotential height from the GFS was used to prescribe $\phi$ on the lateral boundaries as a Dirichlet boundary condition. The boundary $\psi$ was specified using a Neumann boundary condition such that (1) the component of the wind from the GFS analysis perpendicular to the boundary was equivalent to the gradient of $\psi$ along the boundary and (2) by ensuring that there was no net divergence out of the domain. Hydrostatic balance and the vertically averaged potential temperature, $\theta$, between 1000–950 hPa (100–50 hPa) were used to define a Neumann boundary condition for $\phi$ and $\psi$ on the bottom (top) boundary of the domain. In order to converge on a solution for $\phi$ and $\psi$, negative values of PV were changed to a small positive constant (0.01 PVU; 1 PVU = $10^{-6}$ K m$^2$ kg$^{-1}$ s$^{-1}$) and the static stability was not permitted to become negative.

The methodology for inverting the MPV is identical to the full PV, but with the $\phi$, $\psi$, and $\theta$ fields from the GFS analysis replaced by a 6-day average of those variables, $\bar{\phi}$, $\bar{\psi}$, and $\bar{\theta}$, along the boundaries using a Dirichlet boundary condition. Lateral and horizontal Dirichlet boundary conditions for an inversion of the full PPV, $\phi'$, $\psi'$, and $\theta'$, were specified as the difference between the boundary $\phi$, $\psi$, and $\theta$ from the full PV inversion and the MPV inversion (i.e., $\phi - \bar{\phi} = \phi'$). Lateral Dirichlet boundary conditions, with $\phi' = 0$ and $\psi' = 0$, were established for inversions of the SPV, IPV, UTPV, PJPV, and STJPV, while $\theta'$ at the top and bottom boundaries

298 for these inversions was specified using a Dirichlet boundary condition according to the
299 partitioning scheme discussed in Section 2a.

300 A static PV inversion only returns the balanced, non-divergent flow associated with each
301 subset of the PV distribution. Given that vertical motion can also play a substantial role in
302 restructuring the tropopause during a jet superposition event (WM16), recovery of the balanced
303 divergent flow associated with each subset of the PV distribution was also required. This
304 particular task was accomplished by inverting the system of prognostic balance equations
305 described in Davis and Emanuel (1991). This technique returned the geopotential tendency, $\phi^t$,
306 streamfunction tendency, $\psi^t$, PV tendency, $q^t$, velocity potential, $\chi$, and vertical motion, $\omega$,
307 associated with each subset of the PV distribution.

308 Convergence on a solution to the system of prognostic balance equations for this case
309 required using Dirichlet boundary conditions to set the lateral boundaries of $\phi^t$, $\psi^t$, $q^t$, $\chi$, and $\omega$
310 equal to zero, as well as the top and bottom boundaries of $q^t$, $\chi$, and $\omega$ equal to zero. $\phi^t$ and $\psi^t$
311 along the top and bottom boundaries were determined using a Neumann boundary condition by
312 calculating the time tendency of the hydrostatic equation and the potential temperature tendency,
313 $\theta^t$. The latent heating term ($d\theta/dt$) in the system of prognostic balance equations was calculated
314 following the method employed in Emanuel et al. (1987) and Winters and Martin (2014). In
315 order to converge consistently on a solution to the system of prognostic balance equations,
316 smoothing of the individual forcing terms in the $\omega$-equation was required. As for the static PV
317 inversion, the reader is referred to Davis and Emanuel (1991) for more specific information on
318 the system of prognostic balance equations and its inversion.

319 The combination of the static and prognostic PV inversion recovers the balanced three-
320 dimensional flow associated with each subset of the PV distribution. The unbalanced portion of

the flow cannot be returned via these methods and falls into a residual term, which primarily corresponds to the non-divergent component of the ageostrophic wind (e.g., Davis et al. 1996). For the case considered in this study, the unbalanced portion of the flow exceeded 20 m $s^{-1}$ in the immediate vicinity of the developing superposed jet core[3] and was aligned anti-parallel to, and was considerably weaker than, the balanced non-divergent wind (not shown). Consequently, the restructuring of the tropopause accomplished by the unbalanced portion of the flow was greatly overshadowed by that of the balanced flow at all times considered. As a result, the process of superposition, insofar as it depends on rearrangement of the tropopause, was well explained by the balanced portion of the flow.

## 3. Jet Superposition during the 18–20 December 2009 Mid-Atlantic Blizzard

### *a) Case Overview*

The overview that follows mirrors that provided by WM16 and it is reproduced here because of its relevance to the present study. At 0000 UTC 19 December, a confluent flow pattern was situated over the eastern United States at 250 hPa with a PJ (dashed blue line) located[4] in northwesterly flow over the Central Plains and a STJ (red dashed line) extending from Mexico northeastward over the Gulf of Mexico (Fig. 5a). The surface cyclone responsible for producing blizzard conditions across the Mid-Atlantic States was characterized by a minimum sea-level pressure below 1000 hPa and was positioned in a favorable location for continued development beneath the left exit region of the STJ. A vertical cross section through the PJ and STJ highlights the presence of a three-step tropopause structure and demonstrates that the PJ and STJ were clearly distinct structures at this time (Fig. 1a).

[3] Similar to this case, Davis et al. (1996) also noted that the unbalanced winds were maximized on the anticyclonic shear side of an upper-level jet stream in their analysis of the ERICA-IOP-4 storm.

[4] PJ and STJ axes shown in Fig. 5 are identical to those shown in Fig. 5 of WM16. The axes were identified in WM16 by employing the objective jet identification scheme outlined in Winters and Martin (2014).

342 During the intervening 18 h, the PJ intensified and propagated downstream into the base
343 of an upper-level trough centered over the Great Lakes, such that the PJ axis was aligned parallel
344 to the STJ at 1800 UTC 19 December (Fig. 5b). The STJ also intensified during this interval and
345 shifted poleward of its previous position into the southeastern United States. A cross section
346 through both jet structures at this time demonstrates that, while the jet axes were located in closer
347 proximity to one another, a three-step tropopause structure persisted (Fig. 9b). Additionally, the
348 surface cyclone deepened ~8 hPa from the prior time beneath the left exit region of the STJ, as
349 heavy snowfall continued to impact the Mid-Atlantic States in the cyclone's northwest quadrant.
350 By 1200 UTC 20 December, the axis of the PJ shifted southeastward, as the trough over
351 the Great Lakes continued to deepen, and the STJ migrated farther poleward into the
352 southeastern United States. The combination of these displacements resulted in a vertical
353 superposition (yellow line) of the PJ and STJ from southern Georgia northeastward to off the
354 coast of North Carolina (Fig. 5c). A cross section through the superposed jet at this time
355 indicates a marked increase in jet wind speeds, intensified upper-tropospheric and lower-
356 stratospheric baroclinicity in the vicinity of the jet core, and the development of a two-step
357 tropopause structure (Fig. 1b). Beneath the left exit region of the superposed jet, the surface
358 cyclone continued to deepen rapidly off the New England coast, reaching a minimum sea-level
359 pressure below 980 hPa. The preceding discussion suggests that this case contains PV
360 perturbations associated with the PJ and STJ, as well as PV perturbations associated with the
361 surface cyclone and its extensive precipitation shield. Consequently, it is prudent to consider the
362 role played by each of these PV perturbations during the process of jet superposition.
363 For brevity, the foregoing analysis is restricted to diagnosing the displacement of the
364 tropopause at a single time, 1800 UTC 19 December, 18 h prior to superposition. The results

365 from this time were found to be representative of the entire 36-h period discussed above and
366 permit a synthesis with the previous analysis performed on this case by WM16.

367 *b) Differential Horizontal Displacement of the Tropopause Breaks*

368 As discussed with reference to Fig. 3, both a differential horizontal displacement of the
369 individual tropopause breaks and a vertical displacement of the tropopause steps can contribute
370 to the production of a superposed jet's two-step tropopause structure. To diagnose the three-
371 dimensional displacement of the tropopause, PV advection (PVA) within the domain was
372 calculated by setting all values of PV < 1.5 PVU (> 2.5 PVU) equal to 1.5 PVU (2.5 PVU). This
373 ensures that any diagnosed areas of PVA were restricted to the immediate vicinity of the 2-PVU
374 surface and implied a horizontal or vertical displacement of the tropopause. The subsequent
375 analysis examines the differential horizontal displacement of the polar and subtropical
376 tropopause breaks by calculating PVA within the 1.5–2.5-PVU channel at 300- and 200 hPa,
377 respectively. These isobaric levels are particularly suitable for diagnosing the horizontal
378 displacement of the tropopause since they persistently intersect the polar and subtropical
379 tropopause breaks throughout duration of the case (Fig. 1 and Fig. 9b).

380 The PVA within the 1.5–2.5-PVU channel accomplished along the polar (blue line) and
381 subtropical (red line) tropopause breaks by the balanced non-divergent ($\vec{V}_{nd} = k\times\nabla\psi$) and
382 divergent wind ($\vec{V}_d = \nabla\chi$) at 1800 UTC 19 December is shown in Fig. 6. From this analysis, it is
383 immediately apparent that the non-divergent wind was responsible for a large majority of the
384 PVA diagnosed along each tropopause break. In particular, the polar tropopause break outlined a
385 hook-shaped region of high PV at 300 hPa over the upper Midwest and was characterized by a
386 band of negative PVA (–PVA) by the non-divergent wind from the United States/Canadian
387 border to northern Alabama and a band of positive PVA (+PVA) from the Great Lakes to the

388 Mid-Atlantic States (Fig. 6a). With virtually no PVA provided by the divergent wind at 300 hPa
389 (Fig. 6c), the PVA patterns associated with the non-divergent wind in Fig. 6a implied a
390 downstream propagation of the PV hook at 300 hPa. Importantly, a large section of the polar
391 tropopause break that paralleled the subtropical tropopause break was not characterized by
392 substantial +PVA (Fig. 6a), indicating that the non-divergent wind did not favor a systematic
393 equatorward displacement of the polar tropopause break towards its subtropical counterpart over
394 the southeastern United States at this time.

395 At 200 hPa, the subtropical tropopause break outlined the perimeter of a low-latitude
396 trough west of Mexico and extended northeastward across the Florida peninsula (Fig. 6b).
397 Localized maxima in –PVA by the non-divergent wind characterized the subtropical tropopause
398 break off the coast of South Carolina (Fig. 6b), implying a poleward shift of the subtropical
399 tropopause break towards the polar tropopause break over the Atlantic Ocean. Consequently, this
400 diagnosed poleward movement of the subtropical tropopause break off the South Carolina coast
401 directly contributed to jet superposition 18-h later (Fig. 5c). Farther upstream, an intermittently
402 continuous band of +PVA by the non-divergent wind extended along the subtropical tropopause
403 break from the base of the low-latitude trough west of Mexico northeastward towards the Gulf
404 Coast. While a fraction of the +PVA by the non-divergent wind (Fig. 6b) was offset by a thin
405 strip of –PVA by the divergent wind over the Gulf of Mexico (Fig. 6d), the diagnosed PVA
406 patterns at this time indicated that the subtropical tropopause break would either remain
407 stationary or propagate eastward in locations over the Gulf of Mexico. Consequently, the
408 analysis at this time does not support a vertical superposition of the two tropopause breaks via
409 differential horizontal displacement in locations west of Florida.

410 Given that the non-divergent wind was responsible for a large fraction of the total PVA
411 diagnosed along both tropopause breaks, additional insight is found by partitioning the non-
412 divergent wind field via the piecewise PV inversion techniques described in Section 2. The non-
413 divergent wind and PVA associated with the MPV, UTPV, and IPV are each shown in Fig. 7.
414 The SPV non-divergent wind had a negligible influence on the diagnosed horizontal
415 displacement of the polar and subtropical tropopause breaks during this case and is not included
416 in the subsequent analysis. Figures 7a,b demonstrate that the MPV non-divergent wind was
417 characterized by a confluent flow pattern that accounted for a substantial fraction of the total
418 PVA that was diagnosed along both the polar and subtropical tropopause breaks in Figs. 6a,b.
419 The confluent flow pattern associated with the MPV also conforms well to the conceptual model
420 presented in Fig. 2 and appears to be essential for positioning the polar and subtropical
421 tropopause breaks in close proximity to one another.
422 The UTPV non-divergent wind was characterized by a broad cyclonic circulation that
423 was maximized in the immediate vicinity of the PV hook at 300 hPa (Figs. 7c,d). The UTPV
424 non-divergent wind was responsible for PVA along the polar tropopause break (Fig. 7c) that was
425 of similar magnitude to that forced by the MPV non-divergent wind, but opposite in sign. In
426 particular, the UTPV non-divergent wind was responsible for a strip of –PVA from northern
427 Mississippi to the Mid-Atlantic coast (Fig. 7c) that was collocated with a strip of +PVA by the
428 MPV non-divergent wind (Fig. 7a). Consequently, the competing influence of the UTPV and
429 MPV non-divergent wind resulted in the weak total PVA that was diagnosed along the portion of
430 the polar tropopause break that paralleled the subtropical tropopause break at this time (Fig. 6a).
431 While the MPV non-divergent wind (Fig. 7b) was responsible for a large fraction of the
432 total +PVA diagnosed along the subtropical tropopause break west of the Florida peninsula (Fig.

433 6b), the MPV (Fig. 7b) and UTPV (Fig. 7d) non-divergent wind combined constructively to
434 account for the total –PVA diagnosed east of Florida (Fig. 6b). Specifically, the UTPV non-
435 divergent wind was characterized by southerly flow along the East Coast that resulted in a strip
436 of –PVA east of South Carolina. As a result, both the UTPV and MPV non-divergent wind
437 influenced the diagnosed poleward displacement of the subtropical tropopause break over the
438 Atlantic Ocean (Fig. 6b) that favored a vertical alignment of the two tropopause breaks near that
439 location 18-h later.

440 Figures 7e,f demonstrate the IPV non-divergent flow was characterized by two
441 perturbation anticyclones, with one located east of New England and another situated over the
442 Gulf of Mexico. The perturbation anticyclone east of New England was a direct product of the
443 diabatic erosion of upper-tropospheric PV that accompanied the developing surface cyclone and
444 its extensive precipitation shield (Fig. 5). However, it is apparent at this time that the
445 perturbation anticyclone east of New England was positioned too far downstream to have an
446 influence on the lateral displacement of the polar and subtropical tropopause breaks over the
447 southeastern United States. In contrast, the perturbation anticyclone over the Gulf of Mexico was
448 more favorably located to displace the subtropical tropopause break (Fig. 7f) and was associated
449 with the outflow from persistent tropical convection downstream of the low-latitude trough
450 (WM16; their Figs. 6,8). Despite its favorable location, however, the IPV non-divergent wind
451 only accounted for weak –PVA along the subtropical tropopause break over Mexico (Fig. 7f) and
452 was strongly outweighed by the +PVA accomplished by the MPV non-divergent wind in that
453 same location (Fig. 7b).

454 The substantial influence of the UTPV non-divergent wind on the diagnosed horizontal
455 displacement of the tropopause breaks at this time motivates an examination of the non-divergent

wind associated with the PJPV and STJPV. Recall that the PJPV and STJPV are not a strict partition of the UTPV, but their sum closely approximates the distribution of UTPV. The PJPV non-divergent wind was characterized by a perturbation cyclone that was centered squarely on the PV hook at 300 hPa (Fig. 8a). Furthermore, the non-divergent wind associated with the PJPV was maximized on the southernmost edge of the PV hook at this time, coincident with the location of the PJ axis in Fig. 5b. Figure 8a demonstrates that the PJPV non-divergent wind contributed substantially to the PVA by the UTPV non-divergent wind diagnosed along the polar tropopause break, as well, with PVA of the same sign and in the same locations as shown in Fig. 7c. The strength of the PJPV non-divergent wind was markedly weaker at 200 hPa, however, due to the strong static stability residing above the isentropic layer used to isolate the PJPV (Fig. 4b). Consequently, the PJPV non-divergent wind (Fig. 8b) only accounted for a small fraction of the –PVA by the UTPV non-divergent wind diagnosed along the subtropical tropopause break in Fig. 7d off the coast of South Carolina.

The STJPV non-divergent wind was maximized in the vicinity of the STJ axis along the subtropical tropopause break (Figs. 8c,d) and bore a great deal of qualitative similarity to the UTPV non-divergent wind pattern (Figs. 7c,d). At 300 hPa, the STJPV non-divergent wind was associated with PVA patterns along the polar tropopause break (Fig. 8c) that were nearly identical to those associated with the PJPV (Fig. 8a), which suggests that both the PJPV and STJPV non-divergent wind had a comparable influence on the diagnosed lateral displacement of the polar tropopause break by the UTPV non-divergent wind (Fig. 7c). However, Fig. 8d shows that the STJPV non-divergent wind accounted for nearly all of the PVA by the UTPV non-divergent wind along the subtropical tropopause break in Fig. 7d. As a result, it appears that the

478 non-divergent circulation associated with the STJPV had a greater ability to laterally displace
479 *both* the polar and subtropical tropopause breaks.

480 *c) Vertical Displacement of the Tropopause Breaks*

481 Thus far, the analysis suggests that jet superposition via differential horizontal
482 displacement of the two tropopause breaks was favored off the coast of South Carolina due to
483 contributions from the non-divergent wind associated with the MPV and UTPV, which includes
484 the PJPV and STJPV. Recall from the conceptual model in Fig. 3, however, that vertical motion
485 can also contribute to the production of a jet superposition. Consequently, the analysis must also
486 consider the vertical displacement of the tropopause accomplished by the balanced vertical
487 motion field. The balanced vertical motion field at 1800 UTC 19 December was characterized by
488 a strip of subsidence at 400 hPa that was positioned squarely between the polar and subtropical
489 tropopause breaks (Fig. 9a). Furthermore, a vertical cross section[5], C–C', through both
490 tropopause breaks indicates that the subsidence was positioned directly on and beneath the
491 subtropical tropopause step and polar tropopause break (Fig. 9b). This subsidence was
492 responsible for a band of +PVA along the tropopause that favored a downward displacement of
493 the tropopause and an erosion of the subtropical tropopause step, both of which would contribute
494 to jet superposition.

495 As for the non-divergent wind, the vertical motion can be partitioned by employing a
496 piecewise inversion of the prognostic balance equations. While the MPV non-divergent wind had
497 a substantial influence on horizontally displacing the polar and subtropical tropopause breaks,
498 Fig. 10a indicates that the MPV only accounted for a small fraction of the subsidence diagnosed
499 between the two tropopause breaks. In contrast, the UTPV was associated with a continuous

[5] The subsidence diagnosed along the cross section, C–C', is representative of cross sections in all locations where the polar and subtropical tropopause breaks parallel one another over the southeastern United States and is chosen to match the cross section shown at this time by WM16.

band of subsidence that extended along the polar tropopause break from Kansas to the East Coast (Fig. 10b), most of which was attributable to the PJPV (Fig. 10e) rather than the STJPV (Fig. 10f). The IPV (Fig. 10c) and SPV (Fig. 10d) were also associated with notable subsidence between the two tropopause breaks, with most of the subsidence confined to the southeastern United States and in the immediate vicinity of the surface cyclone. Consequently, the analysis in Fig. 10 suggests that PV perturbations associated with the PJ, the surface cyclone, and the surface cyclone's precipitation shield were most responsible for the production of subsidence that would aid in the development of a jet superposition.

WM16 demonstrated a large fraction of the subsidence observed between the two jet cores at this time was attributable to the ageostrophic transverse circulation associated with the double jet structure (their Figs. 10c,d). An advantage afforded by the piecewise PV inversion techniques employed in this study is the ability to partition the ageostrophic transverse circulation diagnosed by WM16 and to identify the dynamical structures most responsible for its production. The ageostrophic transverse circulation can be partitioned using the piecewise form of the Sawyer–Eliassen circulation equation (Sawyer 1956; Eliassen 1962) proposed by Morgan (1999):

$$\left(\gamma\frac{\partial\theta}{\partial p}\right)\frac{\partial^2\psi_{se}}{\partial y^2}+\left(2\frac{\partial M}{\partial p}\right)\frac{\partial^2\psi_{se}}{\partial y\partial p}+\left(-\frac{\partial M}{\partial y}\right)\frac{\partial^2\psi_{se}}{\partial p^2}=2\gamma\left(\frac{\partial U_g'}{\partial y}\frac{\partial\theta}{\partial x}+\frac{\partial V_g'}{\partial y}\frac{\partial\theta}{\partial y}\right) \quad (1)$$

where γ is a constant on isobaric surfaces [ $\gamma = (R/fp_o)(p_o/p)^{c_v/c_p}$ ], $p_o$=1000 hPa, $c_v$=718 J kg$^{-1}$ K$^{-1}$, $c_p$=1004 J kg$^{-1}$ K$^{-1}$, $R$ is the gas constant for dry air, θ is the potential temperature, and $f$ is the Coriolis parameter. $M$ is defined as the absolute geostrophic momentum and $U_g'$ and $V_g'$ are the perturbation geostrophic wind components recovered from an inversion of a subset of the PV distribution ( $\overrightarrow{V_g'} = \frac{1}{f}\,\hat{k}\times\nabla\phi'$). The ageostrophic transverse circulation lies in a vertical plane

perpendicular to the jet axes and is determined by the Sawyer–Eliassen streamfunction, $\psi_{se}$, such that the across-jet ageostrophic wind and vertical motion are defined as $v_{ag} = -\partial\psi_{se}/\partial p$ and $\omega = dp/dt = \partial\psi_{se}/\partial y$, respectively.

The technique for partitioning the ageostrophic tranverse circulation consists of isolating the geostrophic wind associated with each subset of the PV distribution and using those components of the geostrophic wind to calculate the right hand side of (1). Solution to (1) then proceeds by using the full distribution of $\theta$ and $M$ to calculate the coefficients on the left hand side of (1) and by employing an identical method for inversion as outlined in WM16. Given that all of the operators in (1) are linear, the ageostrophic transverse circulations associated with each subset of the PV distribution add together to produce the full ageostrophic transverse circulation forced by the total geostrophic wind. The reader is referred to Eliassen (1962) or Keyser and Shapiro (1986) for a more detailed discussion of the Sawyer–Eliassen circulation equation and to Morgan (1999) for a discussion on the piecewise form of the equation.

Figure 11a shows the ageostrophic transverse circulation within the cross section, C–C', in Fig. 5b that was calculated using the total geostrophic wind from the full PV inversion. Importantly, the circulation in Fig. 11a is nearly identical that shown in Fig. 10c of WM16, which was computed using the geostrophic wind field from the GFS analysis. The ageostrophic transverse circulation in Fig. 11a was responsible for a substantial fraction of the +PVA diagnosed along the tropopause in Fig. 9b, as the subsidence driven by the ageostrophic transverse circulation was favorably located on and beneath the subtropical tropopause step. A partition of the ageostrophic transverse circulation into the piecewise circulations forced by the MPV (Fig. 11b) and PPV (Fig. 11c) geostrophic wind demonstrates that a majority of the +PVA

544 and subsidence in Fig. 11a was associated with the ageostrophic transverse circulation tied to the
545 PPV.

546 The ageostrophic transverse circulation associated with the PPV can be further
547 partitioned into the individual circulations forced by the UTPV, IPV, and SPV geostrophic wind.
548 Figure 12 indicates that the largest fraction of the PPV's ageostrophic transverse circulation was
549 forced by the UTPV geostrophic wind (Fig. 12a), with minor and negligible contributions from
550 the transverse circulations forced by the IPV (Fig. 12b) and SPV (Fig. 12c) geostrophic wind,
551 respectively[6]. This result aligns well with the partition of the complete vertical motion field
552 shown in Fig. 10, which attributed the greatest amount of subsidence between the polar and
553 subtropical tropopause breaks to the UTPV in the vicinity of the cross section, C–C'. The UTPV
554 transverse circulation (Fig. 12a) can be further divided, approximately, into the ageostrophic
555 transverse circulations associated with the PJPV (Fig. 12d) and STJPV (Fig. 12e). Notably, a
556 comparison between Fig. 12d and Fig. 12e indicates that a greater fraction of the UTPV's
557 ageostrophic transverse circulation was associated with the PJPV. Consequently, the analysis
558 provides additional evidence indicating that the flow associated with the PJPV had a greater
559 ability to vertically restructure the tropopause than the flow associated with the STJPV.

560 **4. Discussion**

561 The preceding analysis provides additional support for the results in WM16 and for the
562 role that vertical motion, and particularly ageostrophic transverse circulations, played in the
563 production of a jet superposition during the 18–20 December 2009 Mid-Atlantic Blizzard. The
564 PV analysis also indicated that differential horizontal displacement of the polar and subtropical
565 tropopause breaks contributed substantially to the development of a jet superposition east of the

[6] Vertical cross sections taken further downstream at this time show much more substantial contributions from the ageostrophic transverse circulations associated with the IPV and SPV, consistent with the analysis in Fig. 10.

566 Florida peninsula. These two processes are summarized succinctly in Fig. 13, which shows both
567 a systematic poleward displacement of the subtropical tropopause break and a steady downward
568 displacement of the subtropical tropopause step during the period 1800 UTC 19 December–1200
569 UTC 20 December. It is noteworthy to mention that, near the end of this 18-h period, the polar
570 tropopause break became characterized by weak total +PVA due the MPV non-divergent wind
571 (not shown). This result encouraged an equatorward displacement of the polar tropopause break
572 and contributed to the completion of jet superposition. Overall, both the movement of the
573 tropopause breaks and the downward displacement of the subtropical tropopause step shown in
574 Fig. 13 are completely in line with the conceptual model presented in Fig. 3.

575 The role played by vertical displacement in this case may not be representative of all
576 superposition cases, however, as it is possible that other cases may be solely characterized by a
577 differential horizontal displacement of the two tropopause breaks. Furthermore, additional cases
578 may be associated with proximate latent heat release that could act to erode PV in the vicinity of
579 the three-step tropopause structure in a manner that encourages jet superposition. Consequently,
580 a more comprehensive examination of superposition events is required to ascertain the mode
581 through which jet superpositions develop most frequently over North America.

582 A novel perspective provided by this analysis was the ability to partition the flow and to
583 attribute the development of a superposed jet to dynamical structures present throughout the
584 troposphere and lower stratosphere during the event. In particular, the MPV non-divergent wind
585 was characterized by a large-scale, confluent flow pattern over the eastern United States that
586 aligned well with the conceptual model presented in Fig. 2. This confluent flow pattern was
587 essential in transporting PV perturbations along both the polar and subtropical waveguides
588 towards middle latitudes where they could interact with one another to restructure the tropopause

589 and produce a superposition. Additional work is underway to examine whether the presence of a
590 large-scale, confluent flow pattern is a common element of jet superposition events over North
591 America and to evaluate the variability in upstream flow patterns that are conducive to jet
592 superpositions. The ability to identify large-scale flow patterns that favor the development of jet
593 superposition events could aid in identifying particular forecast periods that present an increased
594 likelihood for jet superpositions and, consequently, for the development of high-impact weather.
595 Aside from the role played by the MPV non-divergent wind, the three-dimensional
596 circulation associated with the UTPV accounted for the largest fraction of the total PVA
597 diagnosed along the tropopause at 1800 UTC 19 December. This result implies that PV
598 perturbations associated with the PJ and STJ had the greatest influence on restructuring the
599 tropopause during the event. While the IPV and SPV non-divergent wind did not impact the
600 horizontal displacement of the tropopause breaks, the IPV and SPV contributed to the subsidence
601 diagnosed between the two tropopause breaks. Consequently, the surface cyclone off the East
602 Coast, and its associated diabatic heating, played a less substantial, though important role in the
603 development of the superposition.
604 It is possible, however, that the SPV and IPV may play a larger role in restructuring the
605 tropopause during superposition cases with more intense cyclogenesis and proximate latent heat
606 release. Furthermore, the influence of the divergent wind was found to be minimal during the
607 18–20 December 2009 Blizzard. However, WM16 demonstrated that cases with extensive
608 midlatitude convection in the vicinity of a double jet structure, such as the 1–3 May 2010
609 Nashville Flood, can be characterized by much stronger horizontal displacement of the
610 tropopause by the upper-tropospheric divergent wind. Consequently, a greater sampling of jet

611 superposition events is required to describe the characteristic types of interactions between PV
612 perturbations during jet superposition events.
613 The substantial role played by the three-dimensional circulation associated with the
614 UTPV in this case motivated isolating the influence of PV perturbations associated with the PJ
615 and STJ. Interestingly, the analysis demonstrated that the STJPV non-divergent wind had a
616 stronger ability to *horizontally* restructure the tropopause than the PJPV non-divergent wind.
617 Physically, the PJPV non-divergent wind was limited in its ability to displace the subtropical
618 tropopause break because of the strong static stability residing above the isentropic layer used to
619 isolate PV perturbations associated with the PJ (Fig. 4). Consequently, the penetration depth of
620 the PJPV's non-divergent circulation above the polar tropopause break was extremely shallow.
621 In contrast, the STJPV's non-divergent circulation was characterized by a deeper penetration
622 depth below the isentropic layer used to isolate PV perturbations associated with the STJ, given
623 the weaker static stability of the upper troposphere. This contrast in the vertical extent of the
624 non-divergent circulations associated with the PJPV and STJPV permitted the STJPV non-
625 divergent wind to have a stronger influence on horizontally displacing both tropopause breaks.
626 An examination of the vertical motion associated with the PJPV and STJPV indicated
627 that the three-dimensional circulation associated with the PJPV had a stronger ability to
628 *vertically* restructure the tropopause. Some insight into the difference between the vertical
629 motion field associated with the PJPV and STJPV is found by considering the forcing terms on
630 the right hand side of the Sawyer–Eliassen circulation equation. Given that stronger baroclinicity
631 typically resides beneath the PJ, the PJPV geostrophic wind is maximized in the immediate
632 vicinity of the strongest tropospheric baroclinicity, by definition. In contrast, the STJPV's
633 horizontal geostrophic circulation has to penetrate downward and laterally before it can interact

with the strongest baroclinicity. Consequently, the PJPV geostrophic wind forces a stronger response from the Sawyer–Eliassen circulation equation than the STJPV geostrophic wind and, correspondingly, more intense subsidence beneath the subtropical tropopause step. The results from this case imply broadly that PV perturbations associated with the PJ and STJ may have distinctly different roles with respect to their ability to restructure the tropopause. However, additional evidence is required to verify this suggestion.

Finally, the techniques employed within this study offer a novel perspective from which to examine a number of different tropospheric phenomena. For example, the jet PV partition can be employed to further corroborate the results of Martius et al. (2010), who found that wave activity can be transferred from one waveguide to another, and to more broadly examine the nature of the interaction between the polar and subtropical waveguides. The jet PV partition also holds promise in its ability to interrogate a number of different phenomena that may occur within an environment characterized by multiple jet structures, such as surface cyclogenesis and extratropical transition. Lastly, the piecewise inversion of the Sawyer–Eliassen circulation equation employed in this study has the potential to provide richer detail into the nature of transverse frontal circulations.

**Acknowledgments**

This work was funded by the National Science Foundation as part of the first author's dissertation research under the grant, AGS-1265182. The authors are grateful for the comments from three anonymous reviewers, whose input has greatly improved this manuscript.

## References


Agusti-Panareda, A., C. D. Thorncroft, G. C. Craig, and S. L. Gray, 2004: The extratropical transition of Hurricane Irene (1999): A potential-vorticity perspective. *Quart. J. Roy. Meteor. Soc.*, **130,** 1047–1074.

Ahmadi-Givi, F., G. C. Graig, and R. S. Plant, 2004: The dynamics of a midlatitude cyclone with very strong latent-heat release. *Quart. J. Roy. Meteor. Soc.*, **130,** 295–323.

Archambault, H. M., L. F. Bosart, D. Keyser, and J. M. Cordeira, 2013: A climatological analysis of the extratropical flow response to recurving western North Pacific tropical cyclones. *Mon. Wea. Rev.,* **141,** 2325–2346.

———, D. Keyser, L. F. Bosart, C. A. Davis, and J. M. Cordeira, 2015: A composite perspective of the extratropical flow response to recurving western North Pacific tropical cyclones. *Mon. Wea. Rev.*, **143,** 1122–1141.

Bosart, L. F., G. J. Hakim, K. R. Tyle, M. A. Bedrick, W. E. Bracken, M. J. Dickinson, and D. M. Schultz, 1996: Large-scale antecedent conditions associated with the 12–14 March 1993 cyclone ("Superstorm '93") over eastern North America. *Mon. Wea. Rev.*, **124,** 1865–1891.

Bretherton, F. P., 1966: Critical layer instability in baroclinic flows. *Quart. J. Roy. Meteor. Soc.*, **92,** 325–334.

Cavallo, S. M., and G. J. Hakim, 2010: Composite structure of tropopause polar cyclones. *Mon. Wea. Rev.*, **138,** 3840–3857.

Christenson, C. E., 2013: A synoptic-climatology of northern hemisphere polar and subtropical jet superposition events. M.S. thesis, Department of Atmospheric and Oceanic Sciences, University of Wisconsin–Madison, 62 pp.

680 Davies, H. C., and A. M. Rossa, 1998: PV frontogenesis and upper-tropospheric fronts. *Mon.*
681 *Wea. Rev.*, **126,** 1528–1539.
682 Davis, C. A., and K. E. Emanuel, 1991: Potential vorticity diagnostics of cyclogenesis. *Mon.*
683 *Wea. Rev.*, **119,** 1929–1953.
684 ———, 1992a: A potential vorticity diagnosis of the importance of initial structure and
685 condensational heating in observed cyclogenesis. *Mon. Wea. Rev.*, **120,** 2409–2428.
686 ———, 1992b: Piecewise potential vorticity inversion. *J. Atmos. Sci.*, **49,** 1397–1411.
687 ———, M. T. Stoelinga, and Y.-H. Kuo, 1993: The integrated effect of condensation in
688 numerical simulations of extratropical cyclogenesis. *Mon. Wea. Rev.*, **121,** 2309–2330.
689 ———, E. D. Grell, and M. A. Shapiro, 1996: The balanced dynamical nature of a rapidly
690 intensifying oceanic cyclone. *Mon. Wea. Rev.*, **124,** 3–26.
691 Defant, F., 1959: On hydrodynamic instability caused by an approach of subtropical and
692 polarfront jet stream in northern latitudes before the onset of strong cyclogenesis. *The*
693 *Atmosphere and Sea in Motion,* New York, Rockefeller and Oxford University Presses,
694 305–325.
695 Eliassen, A., 1962: On the vertical circulation in frontal zones. *Geophys. Publ.*, **24,** 147–160.
696 Emanuel, K. A., M. Fantini, and A. J. Thorpe, 1987: Baroclinic instability in an environment of
697 small stability to slantwise moist convection. Part I: Two-dimensional models. *J. Atmos.*
698 *Sci.*, **44,** 1559–1573.
699 Ertel, H., 1942: Ein neuer hydrodynamischer wirbelsatz. *Meteor. Z.*, **59,** 271–281.
700 Fröhlich, L., P. Knippertz, A. H. Fink, and E. Hohberger, 2013: An objective climatology of
701 tropical plumes. *J. Climate*, **26,** 5044–5060.

Grams, C. M., H. Wernli, M. Böttcher, J. Čampa, U. Corsmeier, S. C. Jones, J. H. Keller, C.-J. Lenz, and L. Wiegand, 2011: The key role of diabatic processes in modifying the upper-tropospheric wave guide: A North Atlantic case-study. *Quart. J. Roy. Meteor. Soc.*, **137,** 2174–2193.

———, S. C. Jones, C. A. Davis, P. A. Harr, and M. Weissmann, 2013: The impact of Typhoon Jangmi (2008) on the midlatitude flow. Part I: Upper-level ridgebuilding and modification of the jet. *Quart. J. Roy. Meteor. Soc.,* **139,** 2148–2164.

Hakim, G. J., L. F. Bosart, and D. Keyser, 1995: The Ohio Valley wave-merger cyclogenesis event of 25–26 January 1978. Part I: Multiscale case study. *Mon. Wea. Rev.,* **123,** 2663–2692.

———, D. Keyser, and L. F. Bosart, 1996: The Ohio Valley wave merger cyclogenesis event of 25–26 January 1978. Part II: Diagnosis using quasigeostrophic potential vorticity inversion. *Mon. Wea. Rev.*, **124,** 2176–2205.

Holopainen, E. O., and J. Kaurola, 1991: Decomposing the atmospheric flow using potential vorticity framework. *J. Atmos. Sci.*, **48,** 2614–2625.

Hoskins, B. J., M. E. McIntyre, and A. W. Robertson, 1985: On the use and significance of isentropic potential vorticity maps. *Quart. J. Roy. Meteor. Soc.*, **111,** 877–946.

———, and P. Berrisford, 1988: A potential vorticity perspective of the storm of 15–16 October 1987. *Weather*, **43,** 122–129.

Iskenderian, H., 1995: A 10-year climatology of Northern Hemisphere tropical cloud plumes and their composite flow patterns. *J. Climate*, **8,** 1630–1637.

Keyser, D., and M. A. Shapiro, 1986: A review of the structure and dynamics of upper-level frontal zones. *Mon. Wea. Rev.*, **114,** 452–499.

725 Korner, S. O., and J. E. Martin, 2000: Piecewise frontogenesis from a potential vorticity
726 perspective: Methodology and a case study. *Mon. Wea. Rev.*, **128,** 1266–1288.
727 Koteswaram, P., 1953: An analysis of the high tropospheric wind circulation over India in
728 winter. *Indian J. Meteor. Geophys.*, **4,** 13–21.
729 ———, and S. Parthasarathy, 1954: The mean jet stream over Indian in the pre-monsoon and
730 post-monsoon seasons and vertical motions associated with subtropical jet streams.
731 *Indian J. Meteor. Geophys.*, **5,** 138–156.
732 Krishnamurti, T. N., 1961: The subtropical jet stream of winter. *J. Meteor.*, **18,** 172–191.
733 Liebmann, B., and D. L. Hartmann, 1984: An observational study of tropical–midlatitude
734 interaction on intraseasonal time scales during winter. *J. Atmos. Sci.*, **41,** 3333–3350.
735 Loewe, F. and V. Radok, 1950: A meridional aerological cross section in the southwest Pacific.
736 *J. Meteor.*, **7,** 58–65.
737 McTaggart-Cowan, R., J. R. Gyakum, and M. K. Yau, 2001: Sensitivity testing of extratropical
738 transitions using potential vorticity inversions to modify initial conditions: Hurricane Earl
739 case study. *Mon. Wea. Rev.*, **129,** 1617–1636.
740 ———, ———, and ———, 2004: The impact of tropical remnants on extratropical
741 cyclogenesis: Case study of Hurricanes Danielle and Earl (1998). *Mon. Wea. Rev.*, **132,**
742 1933–1951.
743 Martius, O., C. Schwiertz, and H. C. Davies, 2010: Tropopause-level waveguides. *J. Atmos. Sci.*,
744 **67,** 866–879.
745 Mohri, K., 1953: On the fields of wind and temperature over Japan and adjacent waters during
746 winter of 1950–1951. *Tellus*, **5,** 340–358.

747 Morgan, M. C., 1999: Using piecewise potential vorticity inversion to diagnose frontogenesis.
748 Part I: A partitioning of the Q vector applied to diagnosing surface frontogenesis and
749 vertical motion. *Mon. Wea. Rev.*, **127,** 2796–2821.
750 ———, and J. W. Nielsen-Gammon, 1998: Using tropopause maps to diagnose midlatitude
751 weather systems. *Mon. Wea. Rev.*, **126,** 241–265.
752 Namias, J., and P. F. Clapp, 1949: Confluence theory of the high tropospheric jet stream. *J.*
753 *Meteor.*, **6,** 330–336.
754 Newell, R. E., N. E. Newell, Y. Zhu, and C. Scott, 1992: Tropospheric rivers? – A pilot study.
755 *Geophys. Res. Lett.*, **19,** 2401–2404.
756 Newton, C. W., 1954: Frontogenesis and frontolysis as a three-dimensional process. *J. Meteor.,*
757 **11,** 449–461.
758 Nielsen-Gammon, J. W., and R. J. Lefevre, 1996: Piecewise tendency diagnosis of dynamical
759 processes governing the development of an upper-tropospheric mobile trough. *J. Atmos.*
760 *Sci.*, **53,** 3120–3142.
761 Palmén, E., and C. W. Newton, 1948: A study of the mean wind and temperature distribution in
762 the vicinity of the polar front in winter. *J. Meteor.*, **5,** 220–226.
763 ———, and ———, 1969: *Atmospheric Circulation Systems: Their Structure and Physical*
764 *Interpretation*. Academic Press, 603 pp.
765 Pyle, M. E., D. Keyser, and L. F. Bosart, 2004: A diagnostic study of jet streaks: Kinematic
766 signatures and relationship to coherent tropopause disturbances. *Mon. Wea. Rev.*, **132,**
767 297–319.

768 Ralph, F. M., P. J. Neiman, and G. A. Wick, 2004: Satellite and CALJET aircraft observations of
769 atmospheric rivers over the eastern North Pacific Ocean during the winter of 1997/98.
770 *Mon. Wea. Rev.*, **132,** 1721–1745.
771 Riehl, H., 1962: Jet streams of the atmosphere. Dept. of Atmospheric Science Tech. Rep. 32,
772 Colorado State University, Fort Collins, CO, 117 pp.
773 Robinson, W. A., 1988: Analysis of LIMS data by potential vorticity inversion. *J. Atmos. Sci.*,
774 **45,** 2319–2342.
775 Roundy, P. E., K. MacRitchie, J. Asuma, and T. Melino, 2010: Modulation of the global
776 atmospheric circulation by combined activity in the Madden–Julian Oscillation and the El
777 Niño/Southern Oscillation during boreal winter. *J. Climate*, **23,** 4045–4059.
778 Sawyer, J. S., 1956: The vertical circulation at meteorological fronts and its relation to
779 frontogenesis. *Proc. Roy. Soc. London*, **234A,** 346–362.
780 Shapiro, L. J., 1996: The motion of Hurricane Gloria: A potential vorticity diagnosis. *Mon. Wea.*
781 *Rev.*, **124,** 2497–2508.
782 ———, and J. L. Franklin, 1999: Potential vorticity asymmetries and tropical cyclone motion.
783 *Mon. Wea. Rev.*, **127,** 124–131.
784 ———, and J. D. Möller, 2003: Influence of atmospheric asymmetries on the intensification of
785 Hurricane Opal: Piecewise PV inversion diagnosis of a GFDL model forecast. *Mon. Wea.*
786 *Rev.*, **131,** 1637–1649.
787 Shapiro, M. A., and D. Keyser, 1990: Fronts, jet streams, and the tropopause. *Extratropical*
788 *Cyclones: The Erik Palmén Memorial Volume,* C. Newton and E. O. Holopainen, Eds.,
789 Amer. Meteor. Soc., 167–191.

790 Sutcliffe, R. C., and J. K. Bannon, 1954: Seasonal changes in the upper-air conditions in the
791 Mediterranean Middle East area. *Proc. Int. Association of Meteorology*, Rome, Italy, Int.
792 Union of Geodesy and Geophysics. 322–334.
793 Thorpe, A. J., 1985: Diagnosis of balanced vortex structure using potential vorticity. *J. Atmos.*
794 *Sci.*, **42,** 397–406.
795 Wandishin, M. S., J. W. Nielsen-Gammon, and D. Keyser, 2000: A potential vorticity diagnostic
796 approach to upper-level frontogenesis within a developing baroclinic wave. *J. Atmos.*
797 *Sci.*, **57,** 3918–3938.
798 Winters, A. C., and J. E. Martin, 2014: The role of a polar/subtropical jet superposition in the
799 May 2010 Nashville Flood. *Wea. Forecasting*, **29,** 954–974.
800 ———, and ———, 2016: Synoptic and mesoscale processes supporting vertical superposition
801 of the polar and subtropical jets in two contrasting cases. *Quart. J. Roy. Meteor. Soc.*,
802 **142,** 1133–1149.
803 Wu, C.-C., and K. A. Emanuel, 1995a: Potential vorticity diagnosis of hurricane movement. Part
804 I: A case study of Hurricane Bob (1991). *Mon. Wea. Rev.*, **123,** 69–92.
805 ———,———, 1995b: Potential vorticity diagnosis of hurricane movement. Part II: Tropical
806 Storm Ana (1991) and Hurricane Andrew (1992). *Mon. Wea. Rev.*, **123,** 93–109.
807 Yeh, T. C., 1950: The circulation of the high tropopause over China in the winter of 1945–46.
808 *Tellus*, **2,** 173–183.
809 Zhu, Y., and R. E. Newell, 1998: A proposed algorithm for moisture fluxes from atmospheric
810 rivers. *Mon. Wea. Rev.*, **126,** 725–735.
811
812

**Figure Captions**

FIG. 1. (a) Vertical cross section, A–A', in Fig. 5a through separate polar and subtropical jet cores at 0000 UTC 19 December 2009, with potential temperature contoured in red every 5-K, wind speed shaded following the legend in m $s^{-1}$, and the 2-PVU surface contoured with the thick blue line. 'PJ' and 'STJ' identify a polar and subtropical jet core, respectively, and the individual tropopause steps are labeled accordingly. (b) As in (a), but for the vertical cross section, B–B' in Fig. 5c, through a superposed jet at 1200 UTC 20 December 2009.

FIG. 2. Conceptual diagram summarizing the development of a jet superposition. The orange arrows depict the branches of an ageostrophic transverse circulation, the green circle identifies an area of convection, and the + (–) symbol corresponds to the center of a polar cyclonic (tropical anticyclonic) PV perturbation, with the blue (red) arrow indicating the movement that particular perturbation towards middle latitudes. The purple fill pattern corresponds to isotachs, with the darker shade of purple identifying faster wind speeds. The locations of the polar jet ('PJ'), subtropical jet ('STJ'), and superposed jets are labeled accordingly. For additional information on interpretation, please refer to the discussion in the text.

FIG. 3. Conceptual diagram illustrating the two ways a three-step tropopause can be restructured into the two-step tropopause characteristic of a superposed jet. The thick black line corresponds to the 2-PVU surface within the cross section, A–A', in Fig. 5a, with the gray shading identifying the stratosphere. The red arrows correspond to the horizontal displacement of an individual tropopause break and the blue arrows identify a vertical displacement of the subtropical tropopause step.

836

837 FIG. 4. (a) Conceptual schematic of the three-way partitioning scheme for the Perturbation PV
838 overlaid on top of the cross section, A–A', in Fig. 5a. Potential temperature is contoured in red
839 every 5-K, the 2-PVU surface is contoured with the thick black line, and the gray shading
840 identifies the stratosphere. Each box in the cross section corresponds to a subset of the PV
841 distribution and is drawn such that the top and bottom boundaries of the box identify the isobaric
842 layer used to isolate that subset of the PV distribution. The relative humidity (RH) criterion also
843 used to isolate each subset of the PV distribution is provided within each box. (b) Similar
844 conventions as in (a) but for the jet PV partitioning scheme. The + and – symbols correspond to
845 positive and negative PV perturbations, respectively, and the locations of the polar ('PJ') and
846 subtropical ('STJ') jets are labeled accordingly. The blue (red) shading identifies the isentropic
847 layer used to isolate the Polar Jet PV (Subtropical Jet PV). (c) Similar conventions as in (b) but
848 with the distribution of Subtropical Jet PV (Polar Jet PV) at 0000 UTC 19 December 2009
849 contoured every 1 PVU in yellow (light blue). Positive (negative) perturbation PV values are
850 denoted by the solid (dashed) contours.
851

852 FIG. 5. 250-hPa wind speed is shaded according to the legend in m $s^{-1}$, 250-hPa geopotential
853 height is contoured in black every 12 dam, sea level pressure is contoured in green every 4 hPa
854 below 1000 hPa, the location of the surface cyclone is identified with the red 'L', the
855 precipitation shield associated with the surface cyclone is shaded in green, and the jet axes are
856 identified according to the legend at (a) 0000 UTC 19 December 2009, (b) 1800 UTC 19
857 December 2009, and (c) 1200 UTC 20 December 2009.
858

FIG. 6. PV advection at 1800 UTC 19 December 2009 within the 1.5–2.5-PVU channel by the non-divergent wind is shaded following the legend in $10^{-5}$ PVU $s^{-1}$ at (a) 300 hPa and (b) 200 hPa, with the non-divergent streamfunction contoured in black every $120\times10^5$ $m^2$ $s^{-1}$. PV advection within the 1.5–2.5-PVU channel by the divergent wind is shaded as in (a,b) at (c) 300 hPa and (d) 200 hPa, with the divergent wind in excess of 5 m $s^{-1}$ plotted with vectors. The 2-PVU surface at 300 hPa (200 hPa) is contoured in all panels with the blue (red) line and corresponds to the location of the polar (subtropical) tropopause break.

FIG. 7. PV advection at 1800 UTC 19 December 2009 within the 1.5–2.5-PVU channel by the non-divergent wind associated with the (a,b) Mean PV, (c,d) Upper-Tropospheric PV, and (e,f) Interior PV at 300 hPa and 200 hPa, respectively. Conventions are identical to those in Fig. 6, except with the streamfunction now contoured in black (negative values dashed) every $120\times10^5$ $m^2$ $s^{-1}$ in (a,b) and every $60\times10^5$ $m^2$ $s^{-1}$ in (c–f). The red 'L's (blue 'H's) correspond to local minima (maxima) in streamfunction.

FIG. 8. PV advection at 1800 UTC 19 December 2009 within the 1.5–2.5-PVU channel by the non-divergent wind associated with the (a,b) Polar Jet PV and (c,d) Subtropical Jet PV at 300 hPa and 200 hPa, respectively. Conventions are identical to those in Fig. 6, except with the streamfunction now contoured in black (negative values dashed) every $30\times10^5$ $m^2$ $s^{-1}$. The red 'L's (blue 'H's) correspond to local minima (maxima) in streamfunction.

FIG. 9. (a) 400-hPa balanced vertical motion shaded according to the legend in dPa $s^{-1}$ at 1800 UTC 19 December 2009. The 2-PVU surface at 300 hPa (200 hPa) is contoured with the blue

882 (red) line and corresponds to the polar (subtropical) tropopause break. (b) Vertical cross section,
883 C–C', in (a), with potential temperature contoured in red every 5-K, wind speeds shaded
884 according to the legend in m $s^{-1}$, subsidence shaded according the legend in dPa $s^{-1}$, the 1.5-PVU
885 surface contoured with the blue line, and PV advection within the 1.5–2.5-PVU channel
886 accomplished by the sum of the vertical motion and horizontal divergent wind fields contoured
887 in yellow (negative values dashed) every $1\times10^{-5}$ PVU $s^{-1}$.
888
889 FIG. 10. 400-hPa balanced vertical motion associated with the (a) Mean PV, (b) Upper-
890 Tropospheric PV, (c) Interior PV, (d) Surface PV, (e) Polar Jet PV, and (f) Subtropical Jet PV at
891 1800 UTC 19 December 2009. Conventions are identical to those in Fig 9a.
892
893 FIG. 11. Vertical cross section, C–C', in Fig. 5b of the Sawyer–Eliassen streamfunction at 1800
894 UTC 19 December 2009 associated with the (a) Full PV, (b) Mean PV, and (c) Perturbation PV,
895 contoured in black (negative values dashed) every 300 m hPa $s^{-1}$, potential temperature
896 contoured in red every 5-K, wind speed shaded according to the legend in m $s^{-1}$, the 1.5-PVU
897 surface contoured in blue, subsidence associated with the Sawyer–Eliassen circulation shaded
898 according to the legend, and PV advection within the 1.5–2.5-PVU channel by the Sawyer–
899 Eliassen circulation contoured in yellow (negative values dashed) every $1\times10^{-5}$ PVU $s^{-1}$. The
900 arrowheads plotted on the streamfunction contours indicate the sense of the Sawyer–Eliassen
901 circulation.
902
903 FIG. 12. Vertical cross section, C–C', in Fig. 5b of the Sawyer–Eliassen streamfunction at 1800
904 UTC 19 December 2009 associated with the (a) Upper-Tropospheric PV, (b) Interior PV, (c)

905 Surface PV, (d) Polar Jet PV, and (e) Subtropical Jet PV, contoured in black (negative values
906 dashed) every 100 m hPa $s^{-1}$. All other conventions are identical to those in Fig. 11, except that
907 PV advection is now contoured in yellow (negative values dashed) every $0.5\times10^{-5}$ PVU $s^{-1}$.
908
909 FIG. 13. Evolution of the 2-PVU surface within the cross section, B–B', in Fig. 5c during the
910 period 1800 UTC 19 December 2009–1200 UTC 20 December 2009.
911
912
913
914
915
916
917
918
919
920
921
922
923
924
925
926
927

## Figures

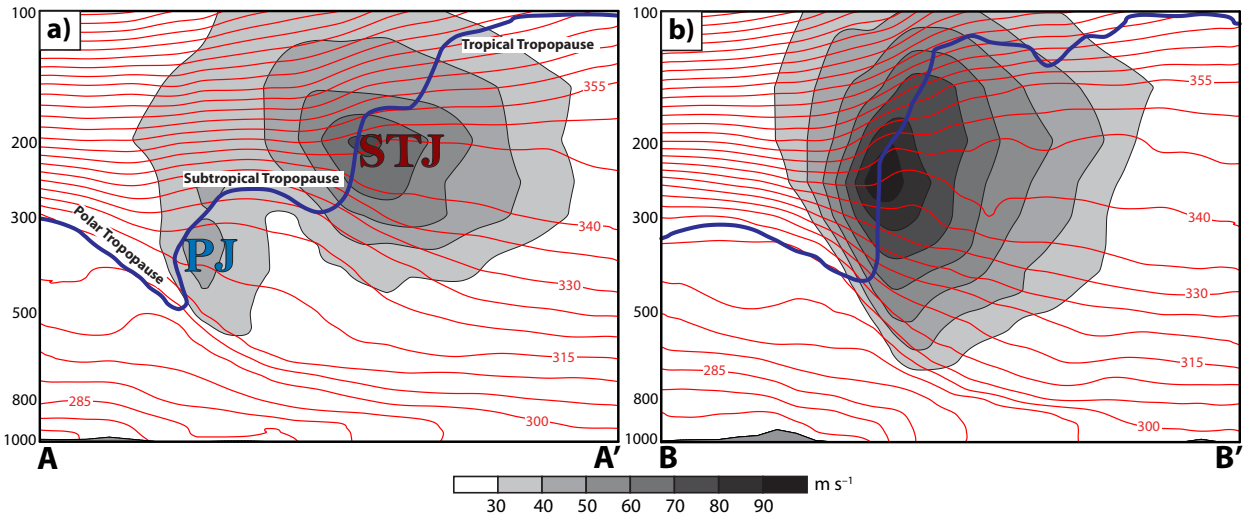


**FIG. 1.** (a) Vertical cross section, A–A', in Fig. 5a through separate polar and subtropical jet cores at 0000 UTC 19 December 2009, with potential temperature contoured in red every 5-K, wind speed shaded following the legend in m $s^{-1}$, and the 2-PVU surface contoured with the thick blue line. 'PJ' and 'STJ' identify a polar and subtropical jet core, respectively, and the individual tropopause steps are labeled accordingly. (b) As in (a), but for the vertical cross section, B–B' in Fig. 5c, through a superposed jet at 1200 UTC 20 December 2009.

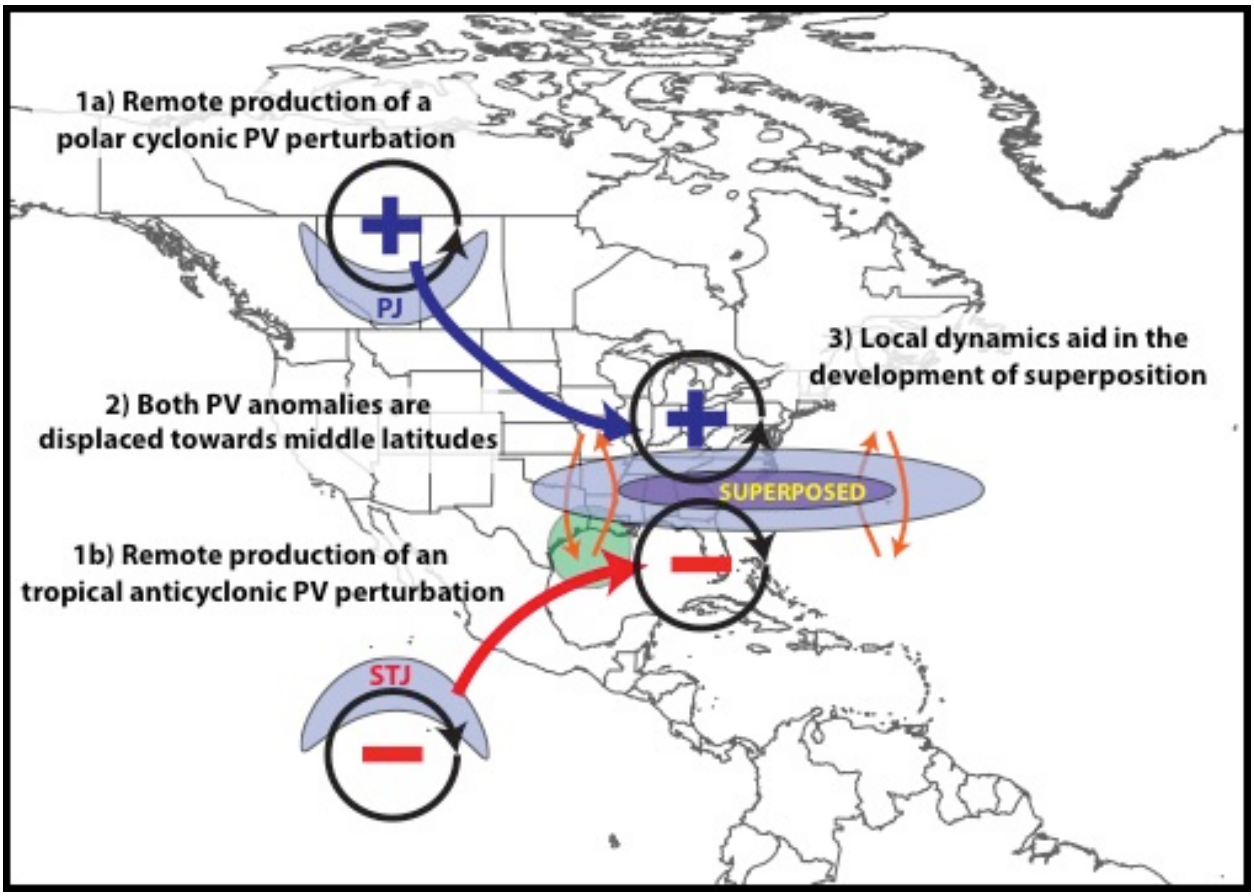


**FIG. 2.** Conceptual diagram summarizing the development of a jet superposition. The orange arrows depict the branches of an ageostrophic transverse circulation, the green circle identifies an area of convection, and the + (–) symbol corresponds to the center of a polar cyclonic (tropical anticyclonic) PV perturbation, with the blue (red) arrow indicating the movement that particular perturbation towards middle latitudes. The purple fill pattern corresponds to isotachs, with the darker shade of purple identifying faster wind speeds. The locations of the polar jet ('PJ'), subtropical jet ('STJ'), and superposed jets are labeled accordingly. For additional information on interpretation, please refer to the discussion in the text.

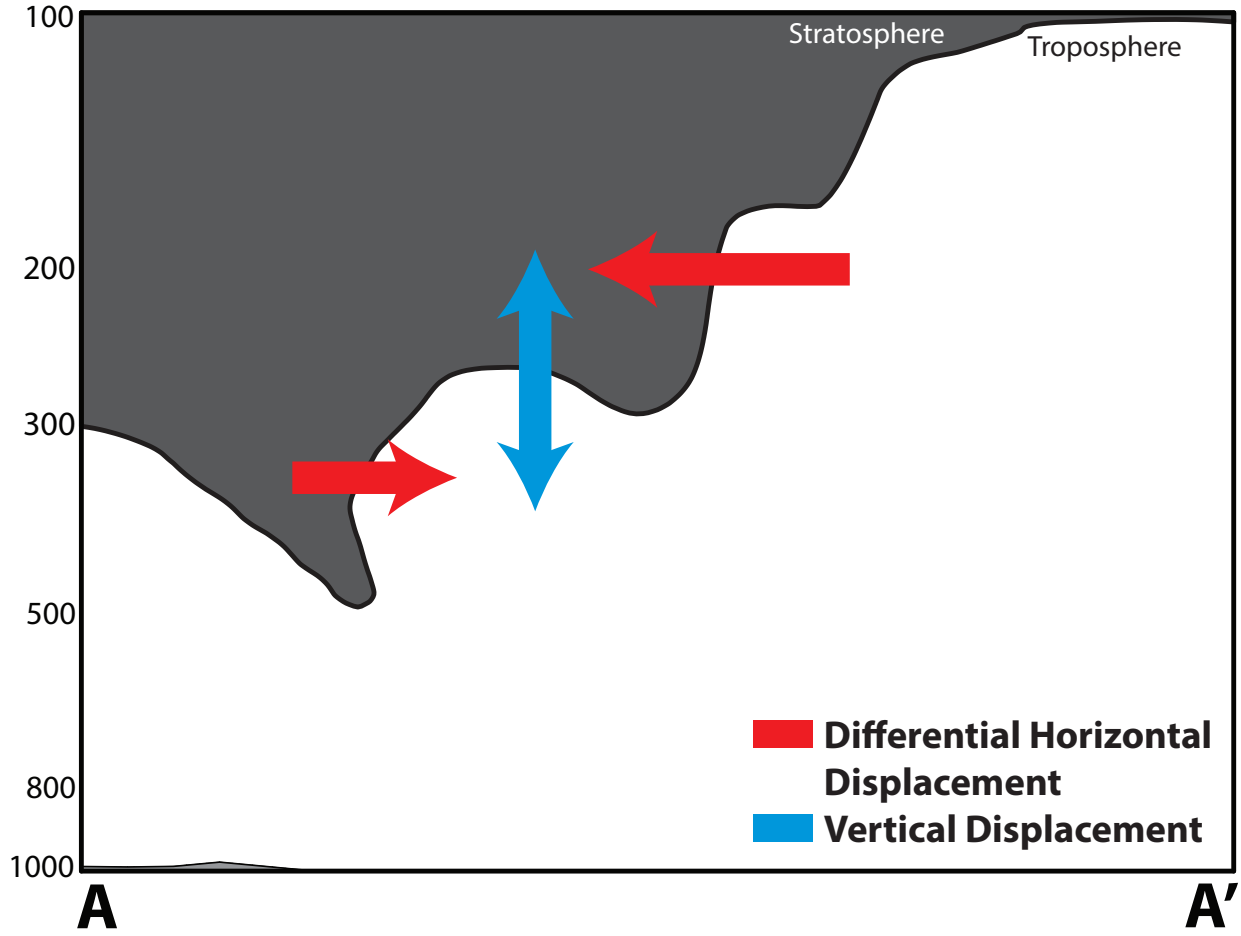


**FIG. 3.** Conceptual diagram illustrating the two ways a three-step tropopause can be restructured into the two-step tropopause characteristic of a superposed jet. The thick black line corresponds to the 2-PVU surface within the cross section, A–A’, in Fig. 5a, with the gray shading identifying the stratosphere. The red arrows correspond to the horizontal displacement of an individual tropopause break and the blue arrows identify a vertical displacement of the subtropical tropopause step.

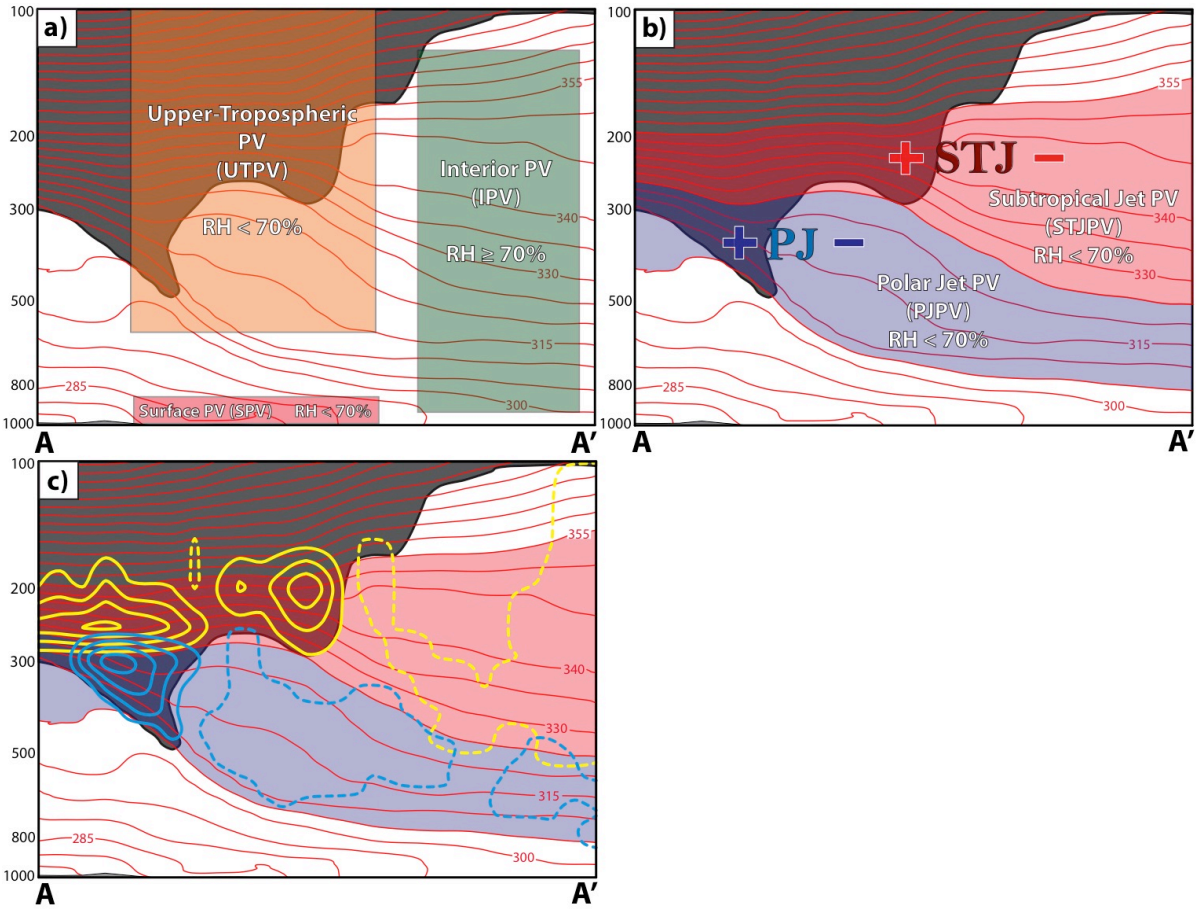


**FIG. 4.** (a) Conceptual schematic of the three-way partitioning scheme for the Perturbation PV overlaid on top of the cross section, A–A', in Fig. 5a. Potential temperature is contoured in red every 5-K, the 2-PVU surface is contoured with the thick black line, and the gray shading identifies the stratosphere. Each box in the cross section corresponds to a subset of the PV distribution and is drawn such that the top and bottom boundaries of the box identify the isobaric layer used to isolate that subset of the PV distribution. The relative humidity (RH) criterion also used to isolate each subset of the PV distribution is provided within each box. (b) Similar conventions as in (a) but for the jet PV partitioning scheme. The + and – symbols correspond to positive and negative PV perturbations, respectively, and the locations of the polar ('PJ') and subtropical ('STJ') jets are labeled accordingly. The blue (red) shading identifies the isentropic layer used to isolate the Polar Jet PV (Subtropical Jet PV). (c) Similar conventions as in (b) but with the distribution of Subtropical Jet PV (Polar Jet PV) at 0000 UTC 19 December 2009 contoured every 1 PVU in yellow (light blue). Positive (negative) perturbation PV values are denoted by the solid (dashed) contours.

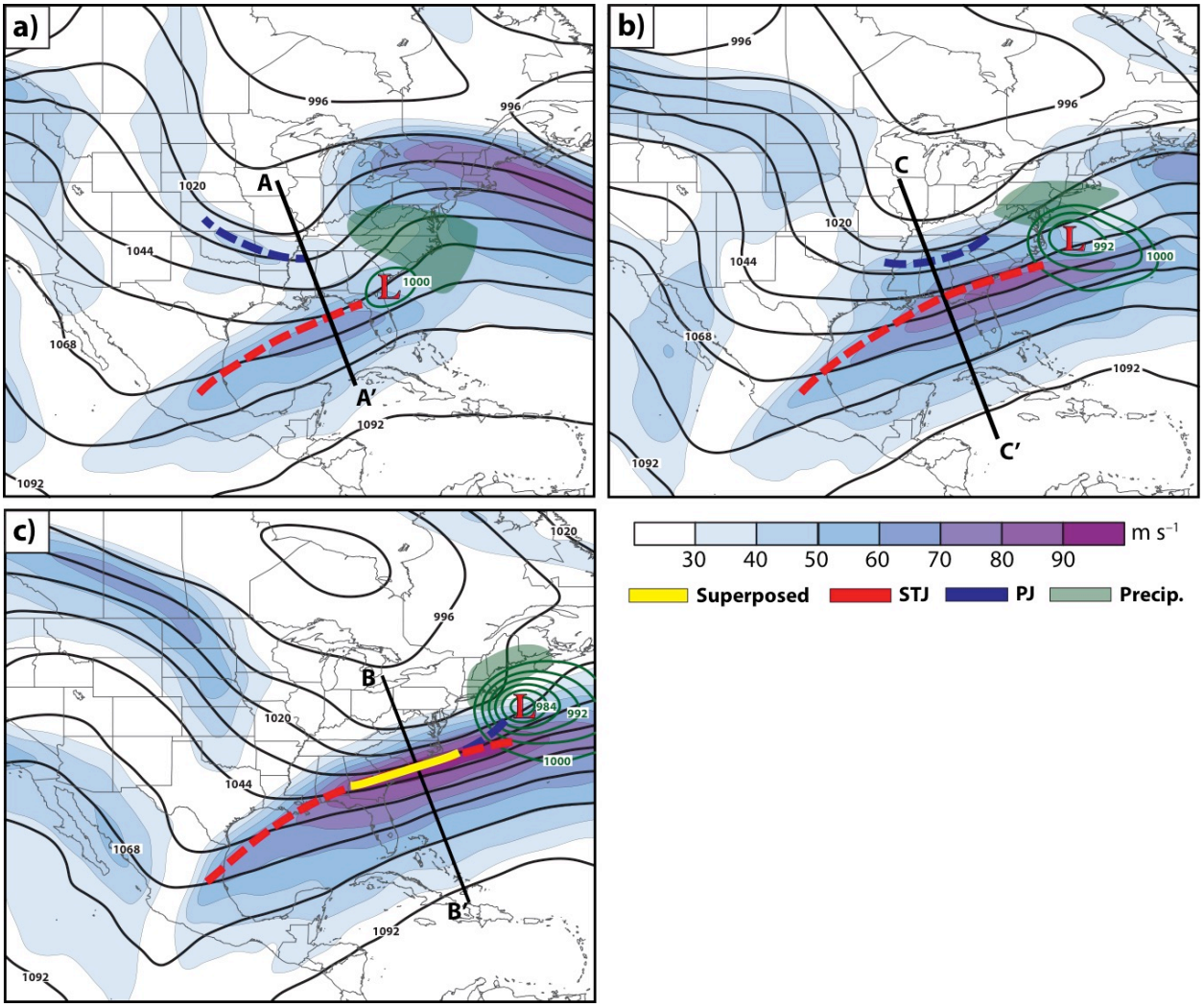


**FIG. 5.** 250-hPa wind speed is shaded according to the legend in m $s^{-1}$, 250-hPa geopotential height is contoured in black every 12 dam, sea level pressure is contoured in green every 4 hPa below 1000 hPa, the location of the surface cyclone is identified with the red 'L', the precipitation shield associated with the surface cyclone is shaded in green, and the jet axes are identified according to the legend at (a) 0000 UTC 19 December 2009, (b) 1800 UTC 19 December 2009, and (c) 1200 UTC 20 December 2009.

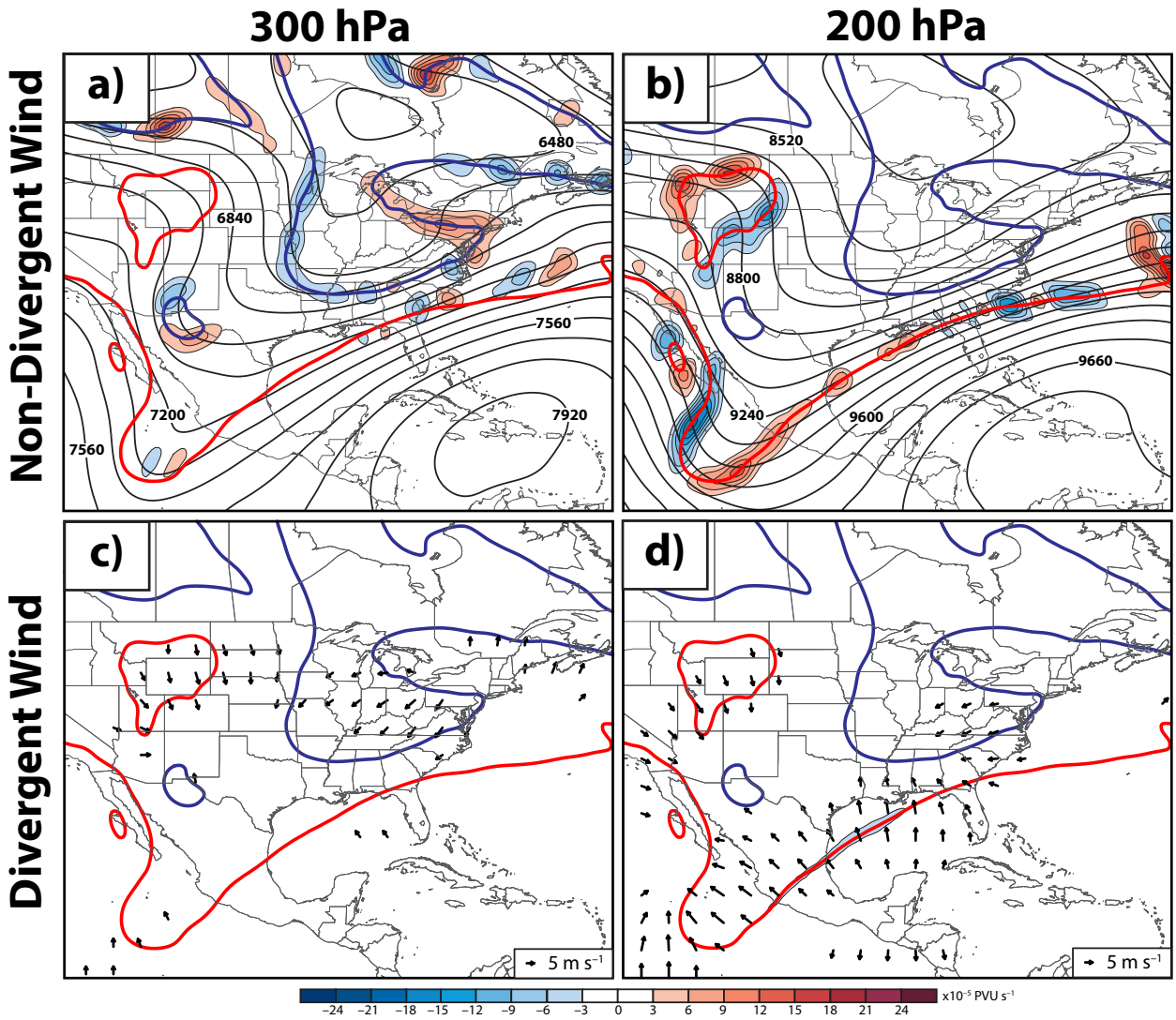


**FIG. 6.** PV advection at 1800 UTC 19 December 2009 within the 1.5–2.5-PVU channel by the non-divergent wind is shaded following the legend in $10^{-5}$ PVU $s^{-1}$ at (a) 300 hPa and (b) 200 hPa, with the non-divergent streamfunction contoured in black every $120\times10^5$ $m^2$ $s^{-1}$. PV advection within the 1.5–2.5-PVU channel by the divergent wind is shaded as in (a,b) at (c) 300 hPa and (d) 200 hPa, with the divergent wind in excess of 5 m $s^{-1}$ plotted with vectors. The 2-PVU surface at 300 hPa (200 hPa) is contoured in all panels with the blue (red) line and corresponds to the location of the polar (subtropical) tropopause break.

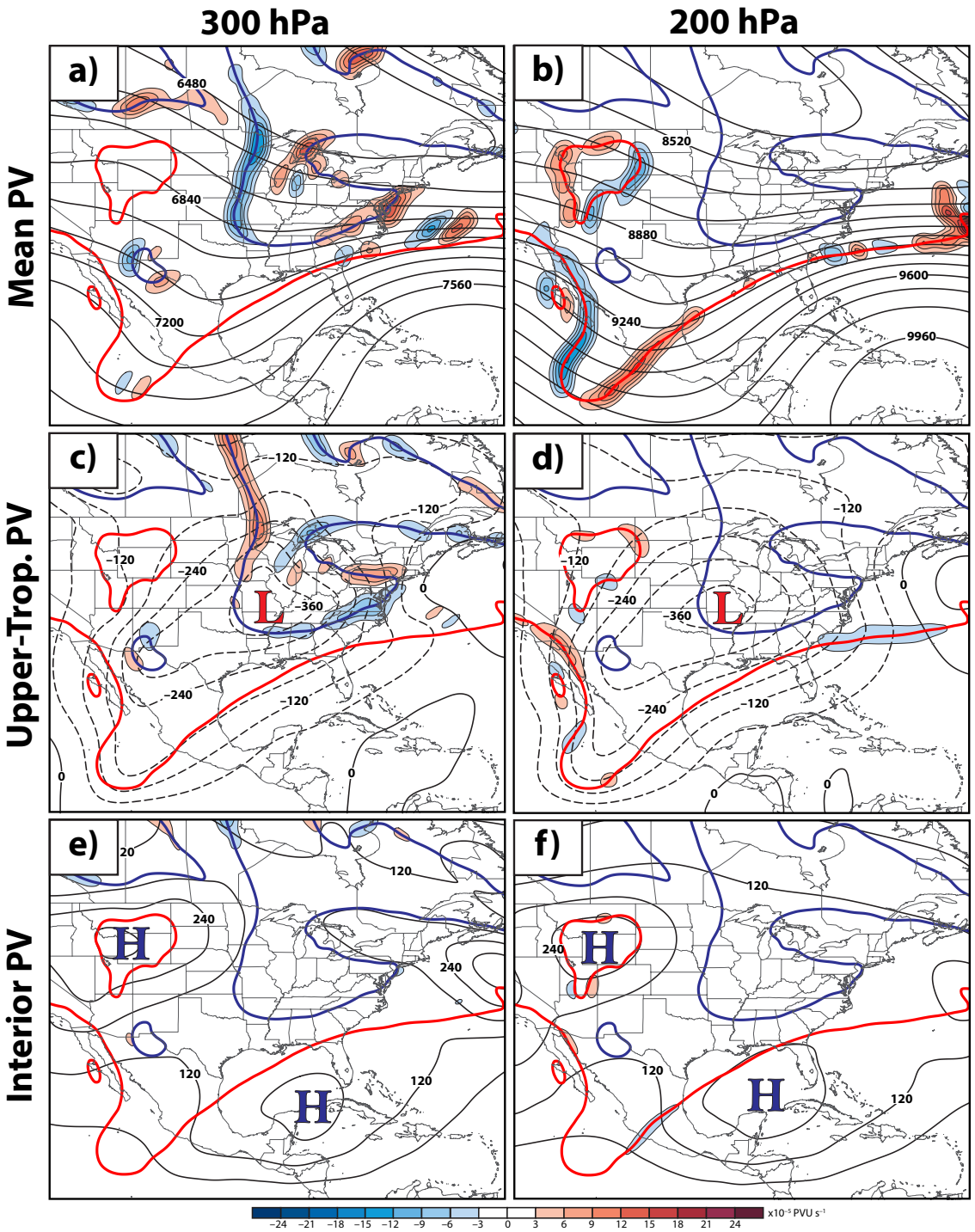


**FIG. 7.** PV advection at 1800 UTC 19 December 2009 within the 1.5–2.5-PVU channel by the non-divergent wind associated with the (a,b) Mean PV, (c,d) Upper-Tropospheric PV, and (e,f) Interior PV at 300 hPa and 200 hPa, respectively. Conventions are identical to those in Fig. 6, except with the streamfunction now contoured in black (negative values dashed) every $120\times10^5$ $m^2$ $s^{-1}$ in (a,b) and every $60\times10^5$ $m^2$ $s^{-1}$ in (c–f). The red 'L's (blue 'H's) correspond to local minima (maxima) in streamfunction.

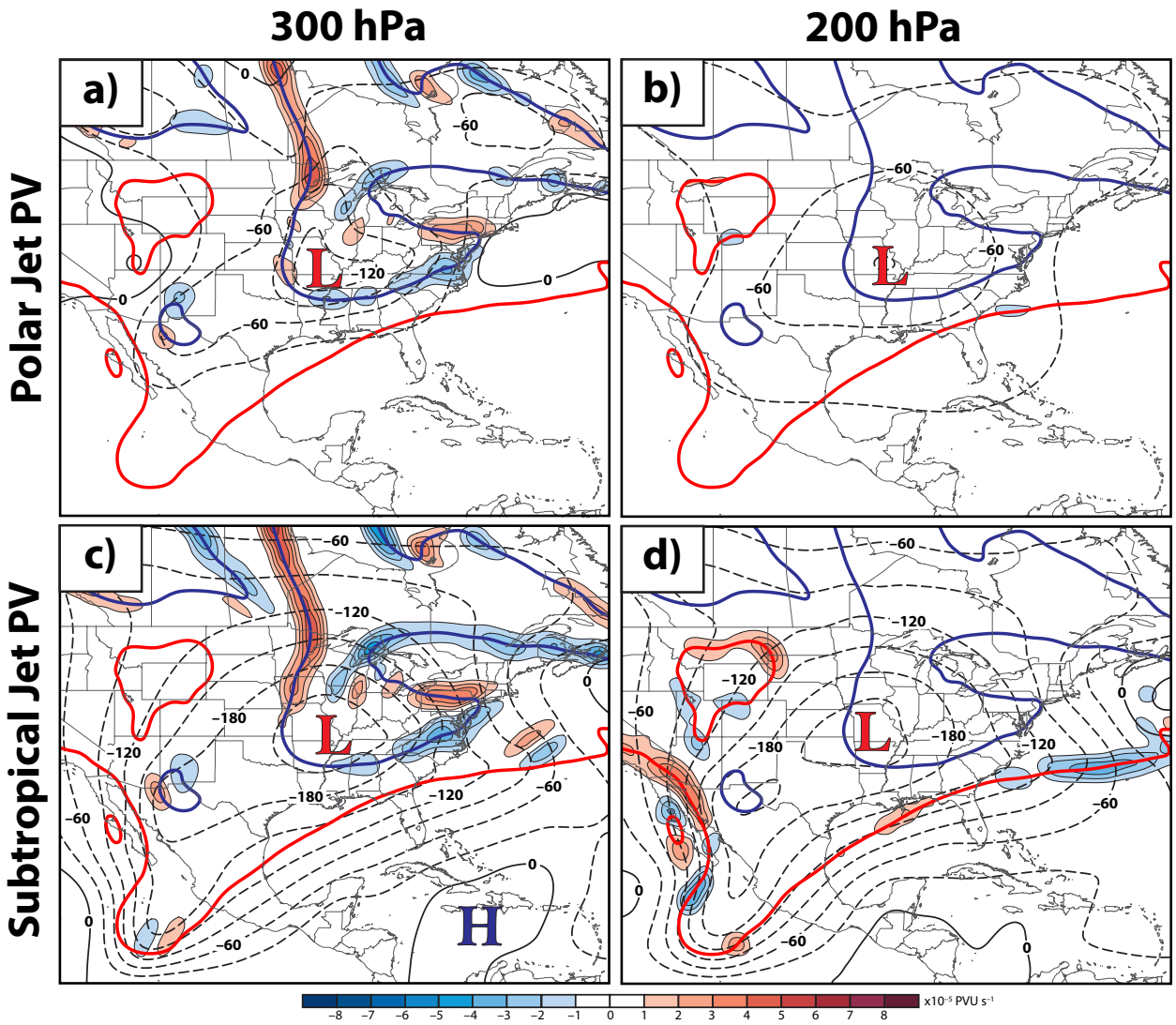


**FIG. 8.** PV advection at 1800 UTC 19 December 2009 within the 1.5–2.5-PVU channel by the non-divergent wind associated with the (a,b) Polar Jet PV and (c,d) Subtropical Jet PV at 300 hPa and 200 hPa, respectively. Conventions are identical to those in Fig. 6, except with the streamfunction now contoured in black (negative values dashed) every $30\times10^5$ m$^2$ s$^{-1}$. The red 'L's (blue 'H's) correspond to local minima (maxima) in streamfunction.

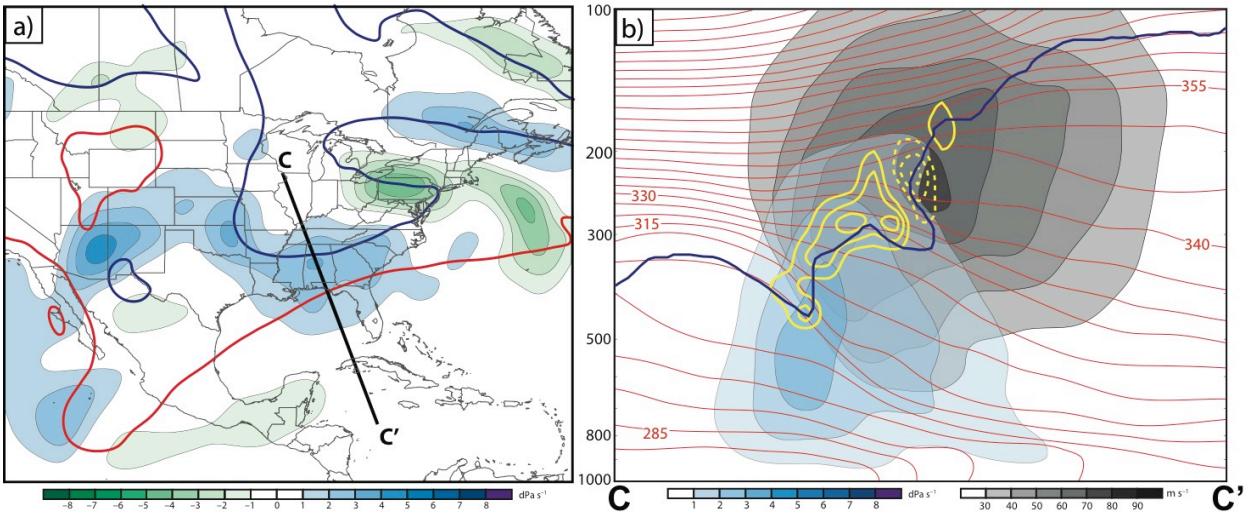


**FIG. 9.** (a) 400-hPa balanced vertical motion shaded according to the legend in dPa $s^{-1}$ at 1800 UTC 19 December 2009. The 2-PVU surface at 300 hPa (200 hPa) is contoured with the blue (red) line and corresponds to the polar (subtropical) tropopause break. (b) Vertical cross section, C–C’, in (a), with potential temperature contoured in red every 5-K, wind speeds shaded according to the legend in m $s^{-1}$, subsidence shaded according the legend in dPa $s^{-1}$, the 1.5-PVU surface contoured with the blue line, and PV advection within the 1.5–2.5-PVU channel accomplished by the sum of the vertical motion and horizontal divergent wind fields contoured in yellow (negative values dashed) every $1\times10^{-5}$ PVU $s^{-1}$.

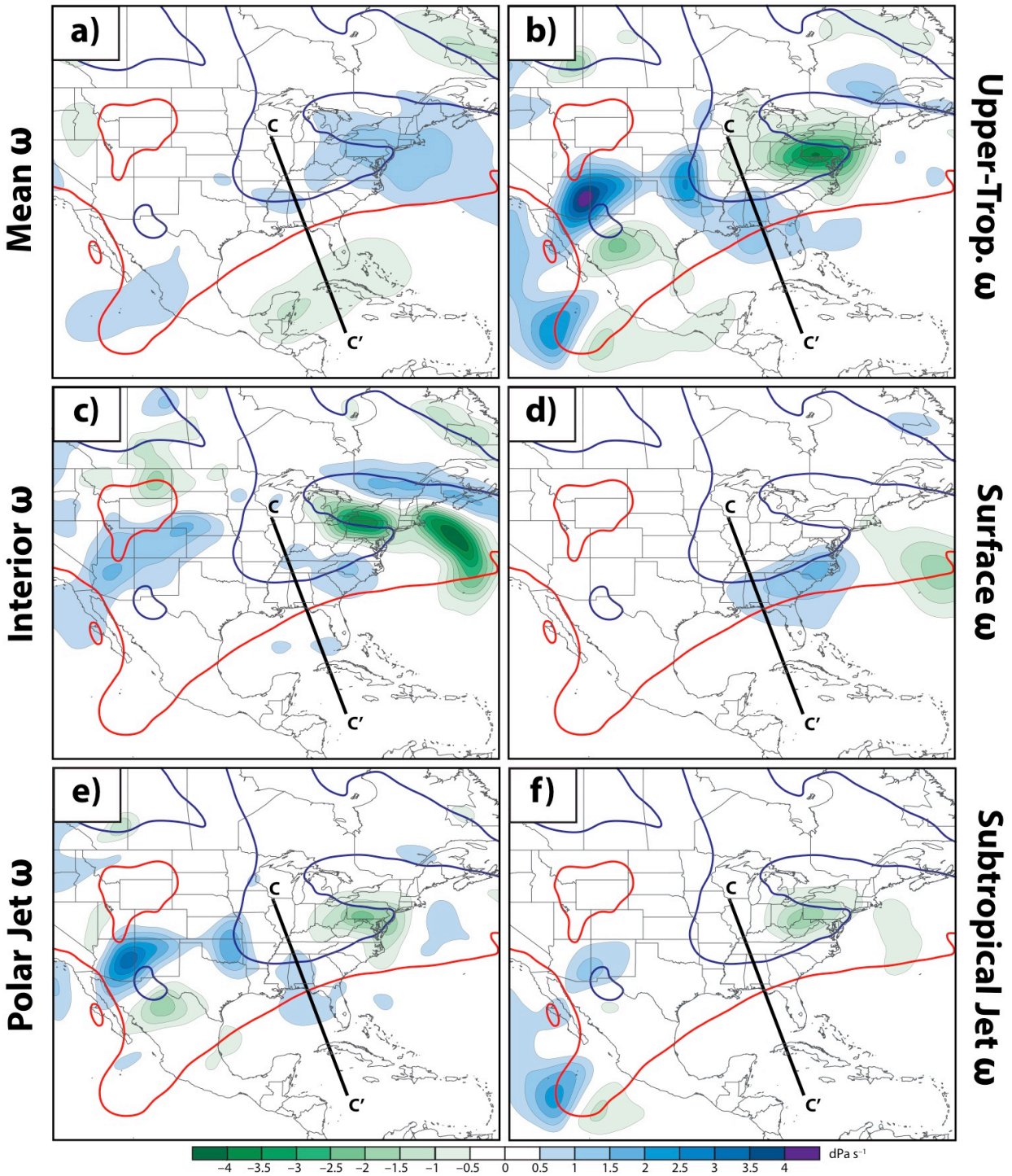


**FIG. 10.** 400-hPa balanced vertical motion associated with the (a) Mean PV, (b) Upper-Tropospheric PV, (c) Interior PV, (d) Surface PV, (e) Polar Jet PV, and (f) Subtropical Jet PV at 1800 UTC 19 December 2009. Conventions are identical to those in Fig 9a.

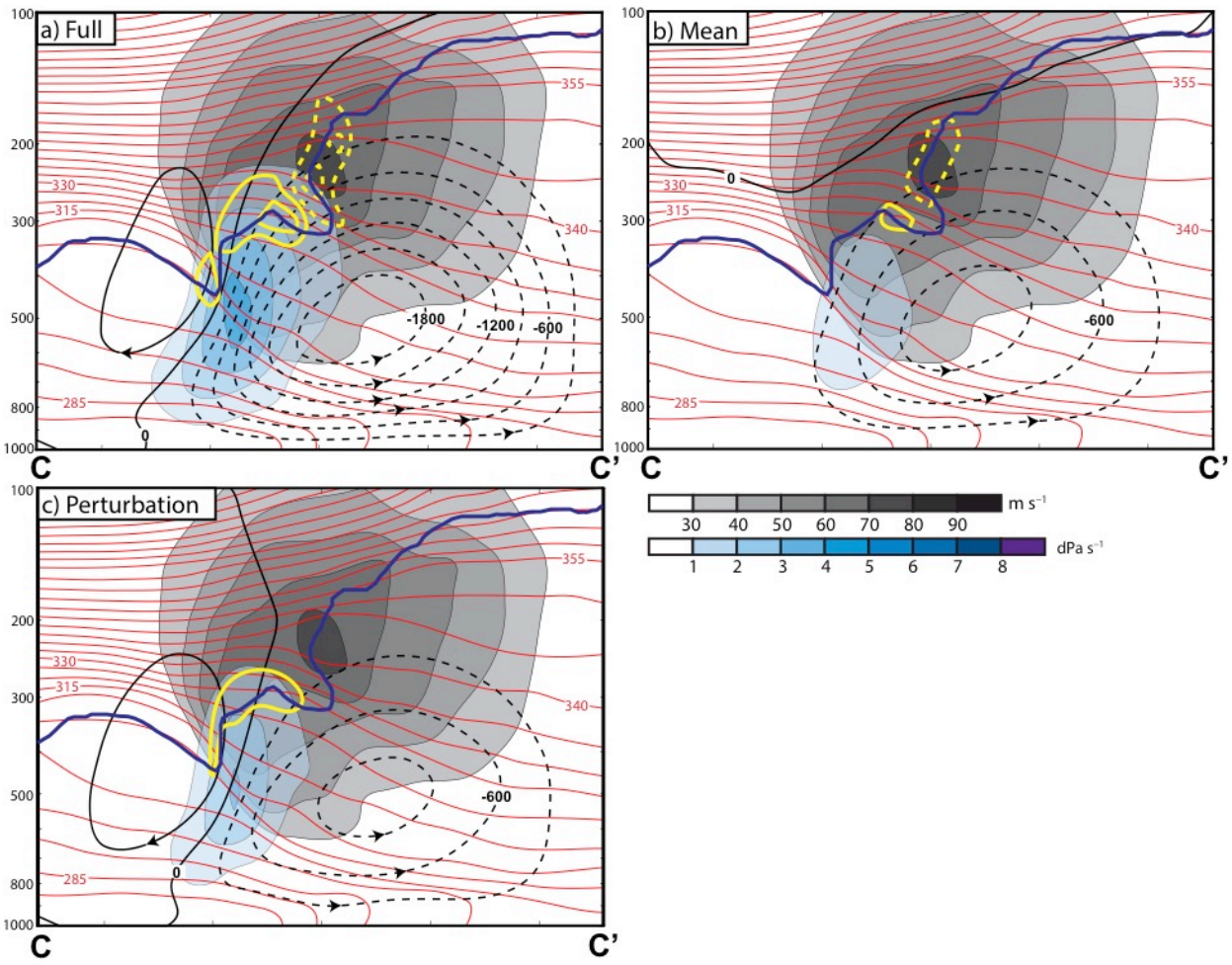


**FIG. 11.** Vertical cross section, C–C', in Fig. 5b of the Sawyer–Eliassen streamfunction at 1800 UTC 19 December 2009 associated with the (a) Full PV, (b) Mean PV, and (c) Perturbation PV, contoured in black (negative values dashed) every 300 m hPa $s^{-1}$, potential temperature contoured in red every 5-K, wind speed shaded according to the legend in m $s^{-1}$, the 1.5-PVU surface contoured in blue, subsidence associated with the Sawyer–Eliassen circulation shaded according to the legend, and PV advection within the 1.5–2.5-PVU channel by the Sawyer–Eliassen circulation contoured in yellow (negative values dashed) every $1\times10^{-5}$ PVU $s^{-1}$. The arrowheads plotted on the streamfunction contours indicate the sense of the Sawyer–Eliassen circulation.

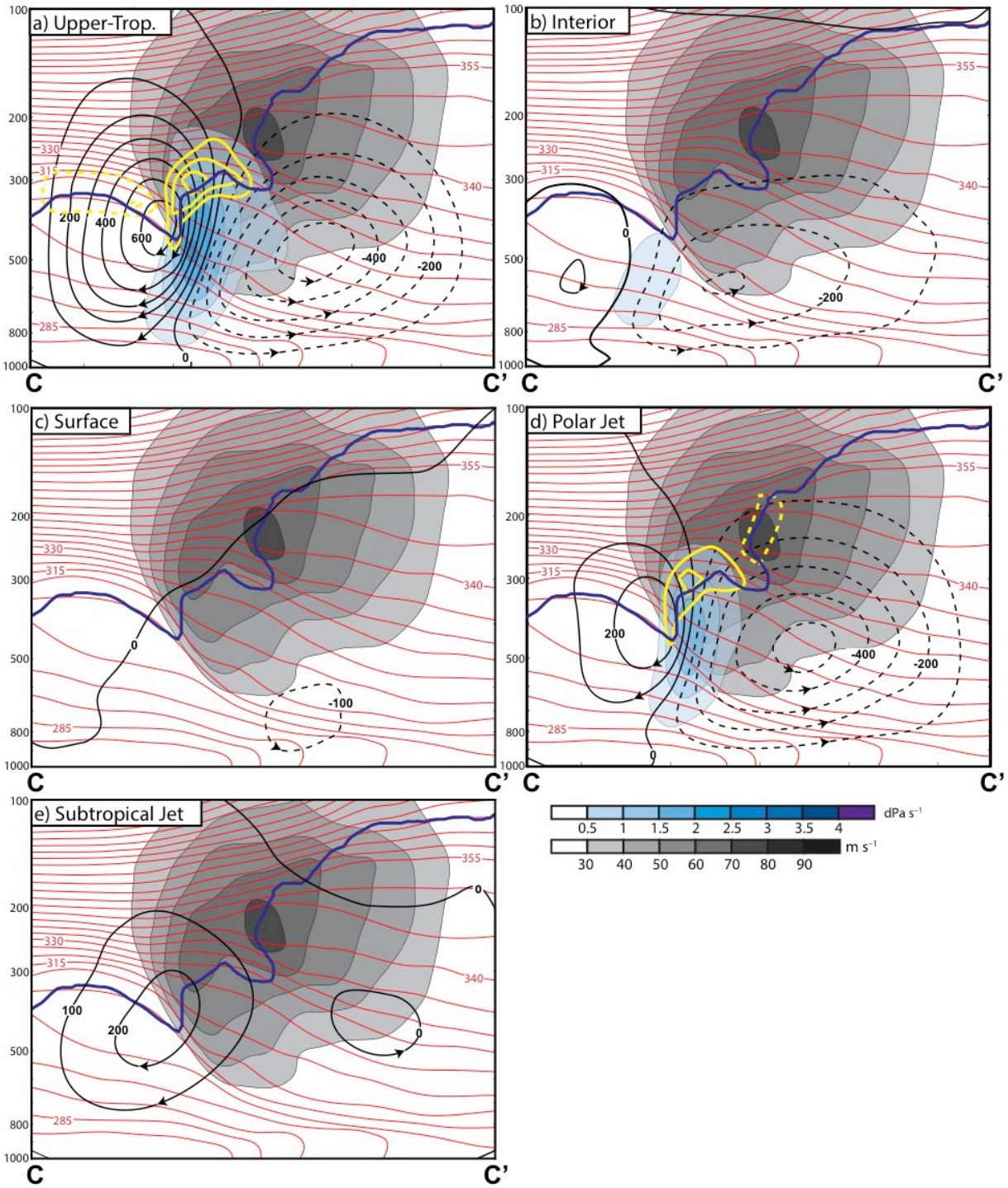


**FIG. 12.** Vertical cross section, C–C', in Fig. 5b of the Sawyer–Eliassen streamfunction at 1800 UTC 19 December 2009 associated with the (a) Upper-Tropospheric PV, (b) Interior PV, (c) Surface PV, (d) Polar Jet PV, and (e) Subtropical Jet PV, contoured in black (negative values dashed) every 100 m hPa $s^{-1}$. All other conventions are identical to those in Fig. 11, except that PV advection is now contoured in yellow (negative values dashed) every $0.5\times10^{-5}$ PVU $s^{-1}$.

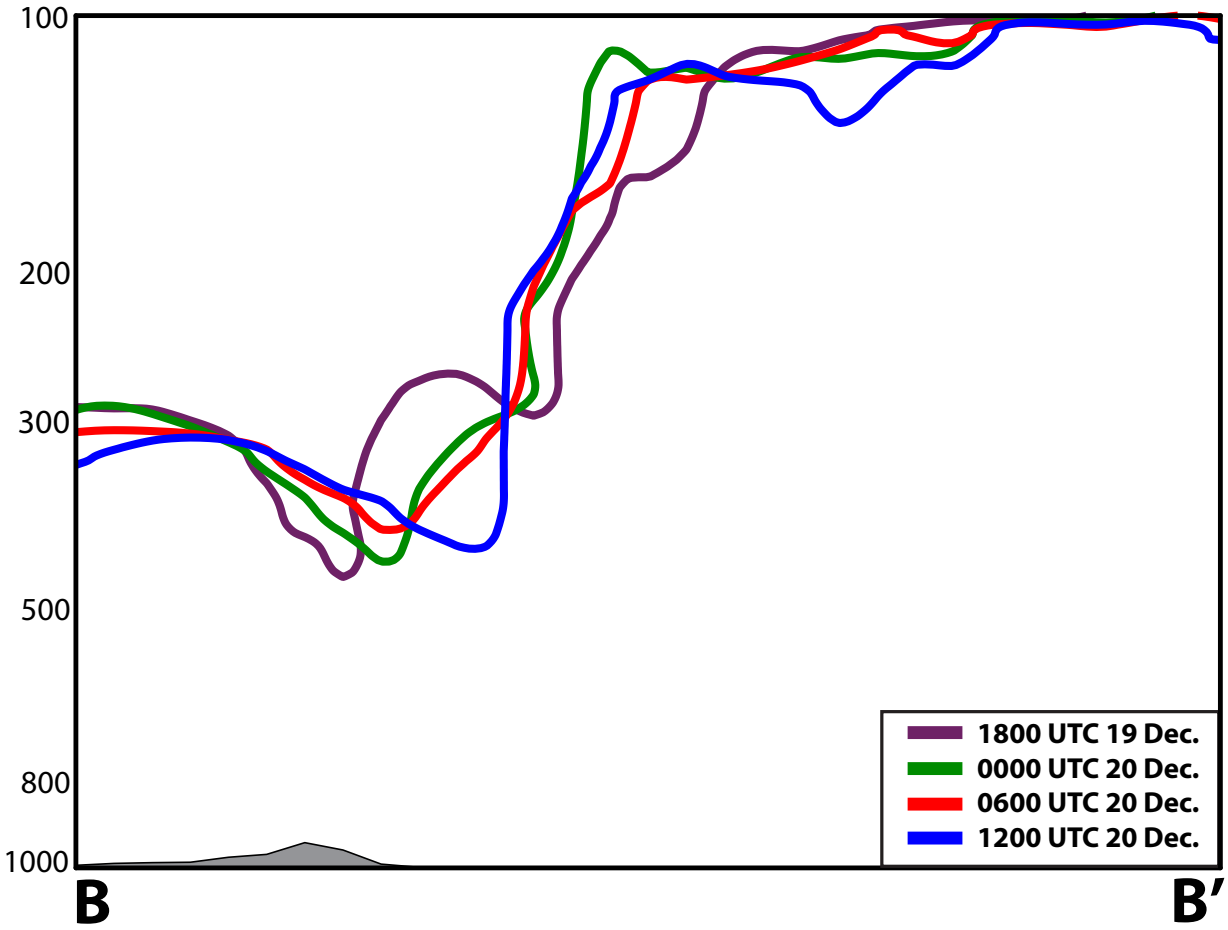


1143
1144 **FIG. 13.** Evolution of the 2-PVU surface within the cross section, B–B', in Fig. 5c during the
1145 period 1800 UTC 19 December 2009–1200 UTC 20 December 2009.
1146